Separation & Purification Reviews
Publication details, including instructions for authors and subscription information:
http://www.informaworld.com/smpp/title~content=t713597294

Modeling of Fouling of Crossflow Microfiltration Membranes

Robert H. Davis[a]
[a] Department of Chemical Engineering, University of Colorado, Boulder, Colorado, USA

To cite this Article Davis, Robert H.(1992) 'Modeling of Fouling of Crossflow Microfiltration Membranes', Separation & Purification Reviews, 21: 2, 75 — 126
To link to this Article: DOI: 10.1080/03602549208021420
URL: http://dx.doi.org/10.1080/03602549208021420

SEPARATION AND PURIFICATION METHODS, 21(2), 75-126 (1992)

MODELING OF FOULING OF CROSSFLOW MICROFILTRATION MEMBRANES

Robert H. Davis
Department of Chemical Engineering
University of Colorado
Boulder, Colorado 80309–0424 USA

Table of Contents

ABSTRACT

Steady-state and transient models are reviewed for predicting flux decline for crossflow microfiltration under conditions in which both external cake buildup and internal membrane fouling are contributing factors. Experimental work is not covered in the scope of this review, although reference is made to a few recent studies which have compared experimental measurements with theory. The steady-state cake thickness and permeate flux are governed by the concentration polarization layer adjacent to the cake of rejected particles which forms on the membrane surface. Depending on the characteristic particle size and the tangential shear rate, Brownian diffusion, shear-induced diffusion, or inertial lift is considered to be the dominant mechanism for particle back-transport in the polarization layer. For typical shear rates, Brownian diffusion is important for submicron particles, inertial lift is important for particles larger than approximately ten microns, and shear-induced diffusion is dominant for intermediate-sized particles. For short times, it is shown that the transient flux decline due to cake buildup is closely approximated by deadend batch filtration theory, independent of the tangential shear rate. For long times, however, the steady or quasi-steady flux increases with shear rate, because the tangential flow sweeps particles toward the filter exit and reduces cake buildup.

1 INTRODUCTION

When pressure–driven flow through a membrane or other filter medium is used to separate particles approximately 0.1–10 μm in size from fluids, then the process is called microfiltration. This size range encompasses a wide variety of natural and industrial particles, including biological cells, clays, paint pigments and polymer latexes. These particles are generally larger than the solutes which are separated by reverse osmosis and ultrafiltration. In consequence, the osmotic pressure for microfiltration is negligible, and the transmembrane pressure drop which drives the microfiltration process is relatively small (less than 50 psi, or 3.4×10^6 g/cm–s^2, typically). Also, the membrane pore size and permeate flux are typically larger for microfiltration than for ultrafiltration and reverse osmosis.

During microfiltration, the imposed pressure drop causes the suspending fluid and small solute species to pass through the membrane or other filter medium and be collected as permeate. The particles are retained by the filter medium and collected as concentrated retentate. The mechanism by which the particles are retained depends on the type of filter medium and the nature of its interactions with the particles being filtered. When a membrane having pores that are smaller than the particles is used to concentrate or clarify a liquid or gas stream, then the sieving mechanism of surface filtration applies. In contrast, a depth filtration mechanism is used in high volume applications such as air filtration in buildings and clean rooms. For the latter, the filter medium is typically a fibrous or granular material which permits particles to enter and adhere to the interior of the filter medium.

Microfiltration processes are traditionally carried out in two types of configurations: deadend and crossflow. In deadend filtration, the pressure–driven suspension flow is perpendicular to the membrane, and the retained particles

build up with time as a cake layer if a membrane, screen, or other surface filter medium is used (see Figure 1a). If a depth filter medium is used, then the retained particles build up in the void spaces. In either case, the particle buildup results in an increased resistance to filtration and causes the permeate flux rate (defined as the volume of permeate formed per unit time per unit membrane area) to decline if the pressure drop is held constant. As a result, the deadend filtration process must be stopped periodically in order to remove the particles or to replace the filter medium, or else the cake must be continuously discharged, such as is done using a knife blade in rotary drum filtration.

During the past two decades, the crossflow configuration has been increasingly used as an attractive alternative to the deadend configuration. For crossflow microfiltration, a membrane is employed as the filter medium, and the sieving mechanism of surface filtration is dominant. The filter operation is similar to that of ultrafiltration and reverse osmosis in that the bulk suspension is made to flow tangential to the surface of the membrane. Although this can be accomplished on a small scale using a batch stir–cell, the common mode of operation is to pump the suspension to be filtered through narrow tubes or channels having microporous membrane walls. The imposed transmembrane pressure drop causes a crossflow of permeate through the membrane to occur. As shown in Figure 1b, the permeate flow carries particles to the membrane surface, where they are rejected and made to form a thin cake layer which is analogous to the gel layer in ultrafiltration. Unlike deadend filtration, this cake layer does not build up indefinitely. Instead, the high shear exerted by the suspension flowing tangential to the membrane surface sweeps the particles toward the filter exit so that the cake layer remains relatively thin. This allows relatively high fluxes to be maintained over prolonged time periods. Theoretical research in the past decade has focused on various mechanisms by which the tangential shear prevents particle deposition on the membrane or cake, leading to models for predicting the permeate flux.

Previous reviews of theory and experiment for crossflow microfiltration have been presented by several authors[1–7]. In the present paper, recent models which

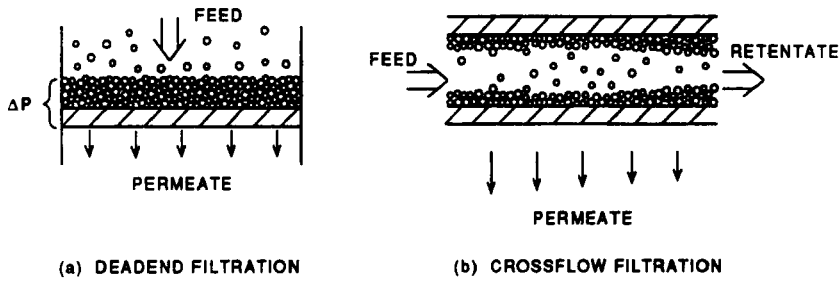

FIGURE 1

Schematics of (a) deadend and (b) crossflow microfiltration.

predict the transient and steady-state permeate flux during crossflow membrane microfiltration are reviewed and compared. The focus is on Brownian diffusion, shear-induced diffusion, and inertial lift. These back-transport mechanisms have received the most attention in the past decade, although alternative mechanisms involving the interaction of individual particles with the cake surface are also being investigated. In Section 2, expressions are given for the steady flux under conditions where very thin fouling layers provide the controlling resistance to filtration. Section 3 examines the situation where thick cake layers with relatively low resistances form adjacent to the membranes, and steady-state models are described which consider the resistance to filtration offered by both the cake layers and the membranes. These concepts are extended in Section 4 to describe the dynamics of flux decline with time due to cake buildup and membrane fouling. Concluding remarks are presented in Section 5.

2 STEADY-STATE MODELS FOR THIN FOULING LAYERS

When the particles being filtered are very small or highly compressible, then a thin fouling layer will quickly form (within a few minutes, or less) within the

interior of the membrane or on its surface. This fouling layer will impart a substantial resistance to filtration, so that the permeate flux quickly reaches a steady or quasi-steady value that is significantly lower than the initial clean membrane flux. The rate at which particles are carried to the membrane surface with the permeate flow is then balanced by back transport of particles away from the membrane surface, and by the convection of these particles toward the filter exit by the suspension flow tangential to the membrane. The back transport mechanisms of Brownian diffusion, shear-induced diffusion, and inertial lift are reviewed and compared in the following subsections. Models involving the interaction of individual particles with the cake or membrane surface are not discussed in detail in this review.

2.1 Brownian Diffusion

It was originally thought that the analogy with ultrafiltration of macromolecules would allow the traditional concentration polarization model (often referred to as "film theory") to predict the steady-state microfiltration flux. In this model, the flux of particles carried toward the membrane by the permeate flow at steady state is balanced by Brownian diffusion and convection away from the membrane, as described by a mass-transfer coefficient[4]. For laminar flow, this approach leads to the following expression for the length-averaged permeate flux:

$$\langle J \rangle = 0.81(\dot{\gamma}_o D_B^2/L)^{1/3} \ln(\phi_w/\phi_b) \quad , \tag{1}$$

where L is the channel length, $\dot{\gamma}_o$ is the shear rate at the surface of the membrane resulting from the bulk laminar flow, D_B is the Brownian diffusivity, and ϕ_b and ϕ_w are the volume fractions of the rejected species in the bulk suspension and at the edge of the fouling layer, respectively. For parabolic laminar flows in narrow tubes or channels, the nominal shear rate at the membrane surface is,

$$\dot{\gamma}_o = 4Q/(\pi H_o^3) \qquad \text{cylindrical tubes} \quad , \tag{2a}$$

$$\dot{\gamma}_o = 3Q/(2WH_o^2) \quad \text{rectangular slits} \quad , \tag{2b}$$

where Q is the volumetric flowrate along the tube or channel, H_o is tube radius or the channel half-height, and W is the channel width. The Brownian diffusivity of a spherical particle in a fluid of viscosity μ_o is given by the Stokes–Einstein relationship:

$$D_B = kT/(6\pi\mu_o a) \quad , \tag{3}$$

where a is the particle radius, T is the absolute temperature, and $k = 1.38\times10^{-16}$ g–cm^2/s^2–K is the Boltzmann constant.

The Lévêque solution on which Eq. (1) is based is strictly valid only when the permeate flux becomes vanishingly small. As a result, Eq. (1) represents an exact solution to the convective diffusion equation only for concentrated suspensions with low fluxes, although it is commonly applied in practice for ultrafiltration over broad concentration ranges. Trettin and Doshi[8] used a similarity solution to derive numerical and asymptotic results for all concentrations. Their solution asymptotes to that given by Eq. (1) for concentrated suspensions ($\phi_w - \phi_b \ll \phi_w$), whereas for dilute solutions ($\phi_b \ll \phi_w$) they showed that

$$\langle J \rangle = 1.31\ (\dot{\gamma}_o D_B^2 \phi_w/\phi_b L)^{1/3} \quad . \tag{4}$$

The particle volume fraction, ϕ_w, in the boundary layer immediately above the thin fouling layer on the membrane may be determined experimentally. Alternatively, if the particles are nonadhesive, then ϕ_w will be equal to the maximum random packing density of particles in the adjacent cake layer, and it may then be estimated that $\phi_w \approx 0.6$ for rigid spherical particles of equal size and $\phi_w \approx 0.8$–0.9 for compressible or polydisperse particles.

Unfortunately, predicted fluxes for micron-sized particles using the Brownian diffusivity given by the Stokes–Einstein relationship were found to be one or more orders-of-magnitude less than those observed in practice[1]. This finding follows from the fact that the Brownian diffusivities of micron-sized particles in water are on the order of 10^{-9} cm^2/s, which is much lower than the molec-

ular diffusivities of macromolecules (yielding lower *predicted* fluxes), whereas the membrane and cake permeabilities for microfiltration are higher than the corresponding permeabilities for ultrafiltration (yielding higher *observed* fluxes). Green and Belfort[9] refer to this discrepancy as the "flux paradox for colloidal suspensions."

2.2 Shear–induced Diffusion

As a possible resolution to the flux paradox, Zydney and Colton[10] proposed that the concentration polarization model could be applied to microfiltration provided that the Brownian diffusivity was replaced by the shear–induced hydrodynamic diffusivity first measured by Eckstein et al.[11] Shear–induced hydrodynamic diffusion of particles occurs because individual particles undergo random displacements from the streamlines in a shear flow as they interact with and tumble over other particles. Zydney and Colton[10] used an approximate relationship for the shear–induced diffusion coefficient measured by Eckstein et al.[11]:

$$D_S = 0.03\ \dot{\gamma}_o a^2 \quad . \tag{5}$$

The shear–induced hydrodynamic diffusivity is proportional to the square of the particle size multiplied by the shear rate, whereas the Brownian diffusivity is independent of shear rate and inversely proportional to particle size. As a result, Brownian diffusion is important for submicron particles and low shear rates, whereas it is dominated by shear–induced hydrodynamic diffusion in typical crossflow microfiltration applications involving micron–sized and larger particles. The shear–induced diffusion coefficient of a micron–sized particle at a modest shear rate of $\dot{\gamma}_o = 1000\ s^{-1}$ is more than two orders–of–magnitude greater than its Brownian diffusivity. Note that the steady–state permeate flux given by Eq. (1) or Eq. (4) becomes proportional to the shear rate when D_S replaces D_B:

$$\langle J \rangle = 0.078\ \dot{\gamma}_o\ (a^4/L)^{1/3} \ln(\phi_w/\phi_b) \qquad \phi_w - \phi_b \ll \phi_w \quad , \tag{6}$$

$$\langle J \rangle = 0.126\ \dot{\gamma}_o\,(\phi_w a^4/\phi_b L)^{1/3} \qquad \phi_b \ll \phi_w \tag{7}$$

Davis and Sherwood[12] have performed an exact similarity solution for the convective–diffusion equation governing the steady–state concentration–polarization boundary layer in crossflow microfiltration of fine particles, under conditions where shear–induced diffusion is the dominant mechanism of particle back–transport. Their solution includes the concentration–dependent shear–induced hydrodynamic diffusivity and effective viscosity of sheared suspensions of spherical particles reported by Leighton and co–workers[13–15]. The result is of similar functional form as are Eqs. (6) and (7), except that the dependence on the particle volume fraction in the bulk solution differs slightly. For dilute suspensions ($\phi_b < 0.1$) of monodisperse rigid spheres which are nonadhesive and have a maximum random packing in the boundary layer of $\phi_w \approx 0.6$, they found that

$$\langle J \rangle = 0.060\ \dot{\gamma}_o\,(a^4/\phi_b L)^{1/3} = 0.072\ \dot{\gamma}_o\,(\phi_w a^4/\phi_b L)^{1/3} \quad , \tag{8}$$

which is identical to Eq. (7), except that the value of the leading coefficient is lower in Eq. (8). The difference is primarily because the concentration–dependent viscosity employed by Davis and Sherwood[12] leads to a lower shear–rate and, hence, decreased shear–induced diffusion in the concentration–polarization boundary layer.

2.3 Inertial Lift

Another proposed resolution of the flux–paradox is that the back–diffusion of particles away from the membrane is supplemented by a lateral migration of particles due to inertial lift[7,9,16–19]. If the conditions are such that the inertial lift velocity is sufficient to offset the opposing permeate velocity, then the particles are not expected to be deposited on the membrane[20]. The inertial lift velocity of spherical particles under laminar flow conditions is of the form

$$v_{L,o} = \frac{b\rho_o a^3 \dot{\gamma}_o^2}{16\ \mu_o} \quad , \tag{9}$$

where ρ_o is the fluid density and b is a dimensionless function of the dimensionless distance from the wall. In the region near the wall, b is positive, indicating that the inertial lift velocity carries the particles away from the wall. Its maximum value near the wall under slow laminar flow conditions (channel Reynolds numbers small compared to unity) is $b = 1.6$ for a slit[21] and $b = 1.3$ for a tube[22]. However, most crossflow filtration operations are carried out under fast laminar flow conditions (channel Reynolds numbers large compared to unity), for which Drew et al.[23] have recently shown that the maximum value is reduced to $b = 0.577$.

The inertial lift velocity increases with the cube of the particle size and the square of the tangential shear rate, and so is expected to be significant for large particles and high flowrates. It is often less than the permeation velocity for micron–sized particles in typical crossflow microfiltration systems[24]. When this is true, a concentrated layer of deposited particles forms on the membrane surface. If this fouling layer has a high resistance, then it will reduce the permeate flux until it just balances the inertial lift velocity. For fast laminar flow with thin fouling layers, the steady–state flux predicted by inertial lift theory is then

$$J = v_{L,o} = 0.036\ \rho_o a^3 \dot{\gamma}_o^2 / \mu_o \quad , \tag{10}$$

which is independent of the filter length and the concentration of particles in the bulk suspension. For nondilute suspensions, however, it is expected that the inertial lift velocity would need to be modified to account for interactions among particles, although this has not been studied to my knowledge.

2.4 Comparison of Different Back–transport Mechanisms

The relative magnitudes of the particle back–transport mechanisms of Brownian diffusion, shear–induced diffusion, and inertial lift depend strongly on the shear–

rate and particle size, and to a lesser extent on the bulk concentration of particles in the feed suspension. When the filtration resistance is controlled by a thin fouling layer, then the steady–state flux is independent of the transmembrane pressure drop and instead is governed by the back–transport mechanism(s) in the concentration–polarization boundary layer. In general, inertial lift is the dominant mechanism for large particles and high shear rates, whereas Brownian diffusion is dominant for small particles and low shear rates. Shear–induced diffusion is most important for intermediate particle sizes and shear rates. This is illustrated quantitatively in Figure 2, where the steady–state flux of water at 20°C versus particle diameter is plotted for a typical shear rate of $\dot{\gamma}_o = 5{,}000$ s^{-1} for each of the three back–transport mechanisms acting independently. It is assumed that the feed suspension is dilute, and so the predicted steady–state fluxes are given by Eqs. (4), (8), and (10), respectively, for Brownian diffusion, shear–induced diffusion, and inertial lift.

From Figure 2, it is seen that Brownian diffusion is only important for particles smaller than about one–half micron in diameter, whereas inertial lift is only important for particles larger than about 20 microns in diameter. The shear–induced diffusion mechanism is dominant for particles with diameters in the intermediate range of $0.5\ \mu m < 2a < 20\ \mu m$, although this range will vary slightly with the system parameters. The predictions of the shear–induced diffusion model have been verified experimentally for cells and particles in this size range by Zydney and Colton[10,24] and Romero and Davis[25].

3 STEADY–STATE MODELS FOR THICK CAKE LAYERS

The results of the previous section are restricted to situations in which a fouling layer which is thin relative to the channel half–height or tube radius provides the

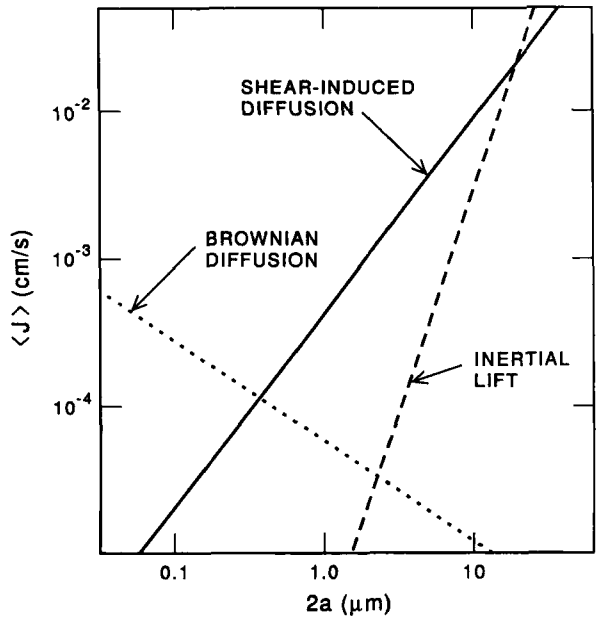

FIGURE 2

Comparison of the predicted steady-state permeate flux versus particle size for Brownian diffusion, shear-induced diffusion, and inertial lift back-transport mechanisms with thin cake layers providing the controlling resistance. The suspending fluid is water at 20°C, and the nominal shear rate is $\dot{\gamma}_o = 5,000\ s^{-1}$.

controlling resistance to filtration. This is generally the case for ultrafiltration of macromolecular solutions and also for microfiltration of suspensions containing very fine colloidal particles or highly deformable particles. However, many microfiltration applications involve nearly rigid particles which are micron-sized or larger. When such particles are rejected by a microporous membrane, they form a cake layer which may have a relatively high permeability (low resistance) due to the ability of the permeate fluid to flow through the interstices between the particles forming the cake. In this case, the cake layer may build up until it occupies a significant fraction of the tube or channel cross-section. Moreover,

both the membrane resistance and the cake resistance may then be important in determining the permeate flux.

The permeate flux may be described by Darcy's law for the cake and membrane resistances in series:

$$J = \frac{\Delta p}{\mu_o (R_m + R_c)} \quad , \tag{11}$$

where μ_o is the permeate (solvent) viscosity, Δp is the transmembrane pressure drop employed between the retentate and permeate sides, R_m is the membrane resistance, and R_c is the cake resistance. For flat cakes, the latter is proportional to the cake thickness or cake mass per unit area:

$$R_c = \hat{R}_c \delta_c = \rho_s (1 - \epsilon_c) R'_c \delta_c \quad , \tag{12a}$$

where $\hat{R}_c$ is the specific cake resistance per unit depth, δ_c is the thickness of the cake layer, R'_c is the specific cake resistance per unit mass per area, ρ_s is the mass density of solid material forming the cake, and ϵ_c is the void fraction of the cake. For cylindrical cakes, this must be modified to take into account the change in cake area with radial position due to curvature:

$$R_c = \hat{R}_c H_o \ln\left(H_o/(H_o - \delta_c)\right) = \rho_s (1 - \epsilon_c) R'_c H_o \ln\left(H_o/(H_o - \delta_c)\right) \quad , \tag{12b}$$

where H_o is the inside radius of the cylindrical tube in the absence of a cake. Compressible cakes, such as flocculated clays or cells, exhibit an increase in their specific resistances with increasing transmembrane pressure. This behavior is often approximated by a power-law function[26]:

$$R'_c = \alpha_o (\Delta p)^s \quad , \tag{13}$$

where α_o is a constant related primarily to the size and shape of the particles forming the cake, and s is the compressibility which varies from zero for incompressible cakes to near unity for highly compressible cakes.

For incompressible cakes, the specific cake resistance may be estimated from the Carman–Kozeny equation[27]:

$$\hat{R}_c = K(1-\epsilon_c)^2 S_c^2/\epsilon_c^3 \quad , \tag{14}$$

where S_c is the solids surface area per unit volume of solids. For uniform spherical particles of radius a, the specific surface area is $S_c = 3/a$, the void fraction is $\epsilon_c = 0.4$, and the leading constant is reported by Grace[28] to have a value of $K = 5$. For a cake composed of micron–sized rigid spheres, the specific cake resistance is estimated from Eq. (14) to be $\hat{R}_c = 10^{11}$ cm^{-2}. For more complex suspensions, the specific cake resistance may be measured experimentally. This is also true of the membrane resistance, since typical membrane morphologies and pore structures may be quite complex. An experimental technique for determining both resistances for a given system is described in Section 5. Typical microfiltration membrane resistances are on the order of $R_m = 10^9 - 10^{10}$ cm^{-1}. The dimensionless parameter $\beta = H_o \hat{R}_c / R_m$ represents the ratio of the resistance of a cake filling the channel to that of the membrane, and it is seen from the above estimates to be approximately 1–10 for micron–sized rigid particles in a 1 mm channel. The value of β is increased for smaller particles and for nonrigid particles which form compressible cakes with high resistances.

In order to use Eqs. (11) and (12) to predict the permeate flux, the thickness of the cake layer which forms on the membrane surface must be known. In general, the cake will build with time until the back transport of particles at its edge just balances the transport of particles to the cake by the permeate flow. In the following two subsections, models are presented to predict the steady–state cake thickness and permeate flux. The first is based on the inertial lift mechanism, which applies for high shear rates and large particles, and the second is based on the shear–induced diffusion model. A similar derivation may be made for back–transport by Brownian diffusion. However, particles which are dominated by Brownian diffusion are usually so small that they form thin cakes with very large resistances, and then the simplified results of Section 2.1 apply.

3.1 Inertial Lift

When applied to crossflow microfiltration, the basic premise of the inertial lift model is that particles are deposited onto the membrane only if the permeate flux exceeds the inertial lift velocity. In this case, a stagnant cake layer will form due to the particle deposition. As the cake layer grows, it reduces the permeate flux due to its resistance. The cake layer also constricts the tube or channel, thereby leading to increases in the shear rate and the inertial lift velocity. The cake continues to build up until the lift velocity, v_L, and the permeate velocity at the edge of the cake layer, v_w, become equal.

The permeate velocity for a cake of thickness δ_c on the membrane is given by Eqs. (11) and (12), together with a mass balance on permeate as it flows through flat or curved cake layers:

$$v_w = J = \frac{J_m}{1+\beta\hat{\delta}} \qquad \text{rectangular slits} \quad , \qquad (15a)$$

$$v_w = \frac{J}{1-\hat{\delta}} = \frac{J_m}{(1-\hat{\delta})(1+\beta\ln(1-\hat{\delta})^{-1})} \qquad \text{cylindrical tubes} \quad , \qquad (15b)$$

where $J_m = \Delta p/\mu_o R_m$ is the permeate flux in the absence of a cake layer and $\hat{\delta} = \delta_c/H_o$ is the dimensionless cake thickness. The inertial lift velocity is given by Eq. (9) but with the shear rate modified to account for the tube or channel being constricted due to the cake buildup. If the feed pump delivers a constant volumetric flowrate, Q, then it is seen from Eq. (2) that the shear rate increases due to a cake buildup of thickness δ_c by a multiplicative factor of $H_o^n/(H_o-\delta_c)^n$, where $n = 3$ for a tube and $n = 2$ for a slit. After taking this into account, the inertial lift velocity is given by

$$v_L = \frac{v_{L,o}}{(1-\hat{\delta})^{2n}} \quad , \qquad (16)$$

where $v_{L,o}$ is the inertial lift velocity given by Eq. (10) for a nonconstricted tube or channel.

Equations (15) and (16) may be solved simultaneously for the permeate flux and cake thickness by setting $v_w = v_L$ at steady state. In the limit of $\beta \gg 1$, a very thin cake layer provides the dominant resistance. The solution of Section 2.3 is then recovered, with the flux given by Eq. (10) and the cake thickness inversely proportional to the specific cake resistance:

$$J = v_{L,o} \quad ; \quad \delta_c = \frac{R_m}{\hat{R}_c}\left(\frac{J_m}{v_{L,o}} - 1\right) \qquad \beta \gg 1 \ , \ J_m > v_{L,o} \quad . \qquad (17)$$

In the opposite limit of $\beta \ll 1$, the membrane provides the controlling resistance. The cake layer then serves to increase the inertial lift velocity by constricting the tube or channel, but it does not affect the permeate flux because of its relatively low resistance:

$$J = J_m = \Delta p/\mu_o R_m \quad ; \quad \delta_c = H_o\left(1 - (v_{L,o}/J_m)^{1/(n+2)}\right) \qquad \beta \ll 1 \quad . \qquad (18)$$

The general solution for various values of the relative cake resistance, β, is shown in Figure 3 as a plot of J/J_m versus $J_m/v_{L,o}$. The steady-state flux increases with increasing $v_{L,o}$ (because of larger inertial lift velocities) and with decreasing β (because thicker cakes form when they have less resistance, and so the inertial lift velocities increase due to channel constriction). As before, the steady-state fluxes predicted by the inertial lift model are independent of the channel length and particle concentration. They are independent of the transmembrane pressure only in the limit $\beta \to \infty$, and become proportional to the transmembrne pressure in the limit $\beta \to 0$. For finite β, the cake layer thickness increases with increasing $J_m/v_{L,o}$, in order to reduce the permeate flux and increase the inertial lift velocity until there is no net particle deposition at the edge of the cake. As $J_m/v_{L,o} \to \infty$, the cake nearly fills the tube or channel; for flat channels the permeate flux then asymptotes to $J = J_m/(1+\beta)$, whereas for cylindrical channels the permeate flux decreases to zero in this limit because the surface area for filtration approaches zero as the cake nearly fills the tube.

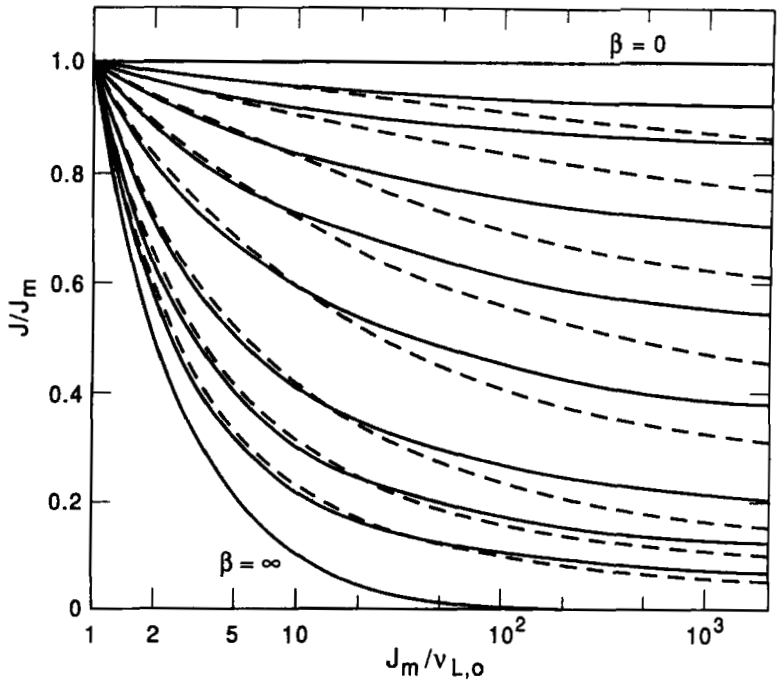

FIGURE 3

The dimensionless permeate flux profile at steady state for inertial lift as the dominant back-transport mechanism. The solid lines are for rectangular filters and the dashed lines are for cylindrical filters. The curves from top to bottom represent $\beta = 0$, 0.1, 0.2, 0.5, 1.0, 2.0, 5.0, 10, 20, and ∞.

3.2 Shear-induced Diffusion

The cake thickness at steady state for diffusive back transport increases with distance from the filter entrance. This thickness is governed by the concentration-polarization boundary layer adjacent to the cake. At a given position x, the polarization layer must transport toward the filter exit all of the particles that are convected into the layer by the permeate flow everywhere upstream of x. The corresponding increase in the cake thickness with x provides for this requirement in two ways. First, the increased cake resistance reduces the local permeate flux,

which allows the concentration polarization layer to expand by diffusion. Second, the increased cake thickness reduces the effective cross–sectional area of the channel so that the suspension velocity (assuming constant flow rate) is increased. These two effects combined lead to an increase with x in the rate at which rejected particles are transported downstream in the polarization boundary layer.

The analysis presented in this section to predict the steady–state cake thickness and permeate flux profiles using the shear–induced diffusion model follows the integral theory first described by Romero and Davis[29]. Modifications are made in order to account for the curvature of the cake layer in cylindrical tubes and for the possibility of partial sticking of the particles at the cake surface. The steady–state integral mass balance on particles in the concentration–polarization layer yields[29]:

$$\int_{\delta_c}^{\delta_c+\delta} u(\phi - \phi_b)dy = \int_o^x v_w \phi_b dx \quad , \tag{19}$$

where v_w is the permeate velocity at the edge of the cake layer, δ is the boundary layer thickness, $\phi(y)$ is the particle volume fraction, $u(y)$ is the velocity in the down–channel (x) direction, and y is the distance measured from the membrane. The first term represents the convection of particles toward the filter exit by the crossflow (the bulk concentration is subtracted from the integral in order to account for the particles present even in the absence of polarization), and the second term represents the convection of particles into the flowing boundary layer by the permeate flow. This equation applies to cylindrical geometries, as well as to rectangular ones, provided that the boundary layer is thin compared to the tube radius. A simple scaling analysis indicates that the boundary thickness is of order D/v_w, and this is typically small compared to H_o for typical conditions encountered in practice. However, $v_w = J$ for rectangular channels, whereas $v_w = JH_o/(H_o - \delta_c)$ for cylindrical tubes from mass balance considerations.

In order to evaluate the first integral in Eq. (19), expressions are needed for the velocity and concentration profiles in the polarization layer. As de-

scribed by Romero and Davis[29], the concentration profile may be determined from a differential mass balance involving convection toward the membrane and diffusion away from the membrane. The axial velocity profile is then found by integrating Newton's viscosity law subject to the assumption of a concentration-dependent Newtonian viscosity and a constant shear stress in the concentration-polarization layer. Davis and Sherwood[12] have shown that this approach, which neglects axial convection in the differential mass balance but retains it when the mass balance is integrated across the polarization boundary layer, is exact in the dilute limit and accurate to within a few percent for nondilute suspensions.

By substituting the resulting velocity profile into Eq. (19), and then using the concentration profile to transform the variable of integration from y to ϕ, the following expression relating the permeate velocity to the boundary layer profiles results:

$$\frac{\mu_b \dot{\gamma}_o H_o^n}{(H_o - \delta_c)^n v_w^2} \int_{\phi_b}^{\phi_w} \int_{\phi}^{\phi_w} \frac{D(\phi')d\phi'}{\phi'\mu(\phi')} \frac{(\phi - \phi_b)D(\phi)d\phi}{\phi} = \int_o^x v_w(x')\phi_b dx' \quad , \quad (20)$$

where $\mu(\phi)$ is the concentration-dependent viscosity of the suspension, $\mu_b = \mu(\phi_b)$ is the viscosity of the bulk suspension, and $D(\phi)$ is the concentration-dependent shear-induced diffusivity. This expression does not apply in a short region near the channel entrance, because axial convection there is sufficient to transport the polarization layer downstream without a stagnant cake forming. This cake-free region extends for $0 \leq x \leq x_{cr}$, where the critical distance is determined from Eq. (20) using $v_w = J_m$ and $\delta_c = 0$:

$$x_{cr} = \frac{\dot{\gamma}_o D_o^2 I_2}{J_m^3 \phi_b} \quad , \quad (21)$$

where the dimensionless function I_2, which is called the crossflow integral, is defined by

$$I_2 = (\mu_b/\mu_o) \int_{\phi_b}^{\phi_w} \int_{\phi}^{\phi_w} \frac{\bar{D}(\phi')d\phi'}{\phi'\bar{\mu}(\phi')} \frac{(\phi - \phi_b)\bar{D}(\phi)d\phi}{\phi} \quad , \quad (22)$$

and $\bar{\mu}(c) = \mu/\mu_o$ and $\bar{D}(c) = (H_o - \delta_c)^n D/H_o^n D_o$ are dimensionless viscosity and diffusivity functions, respectively. The crossflow integral is directly proportional to the dimensionless excess particle flux ($\hat{Q}$) defined previously[15]: $I_2 = (\mu_b/\mu_o)^3\hat{Q}$, and the two are equal in the dilute limit. Numerical values for $\hat{Q}$ are presented by Davis and Leighton[15] using viscosity and diffusivity functions appropriate for suspensions of monodispersed rigid spheres. D_o is a characteristic diffusivity of the particles and is chosen as $D_o = \dot{\gamma}_o a^2$ for shear-induced diffusion. Referring to Eq. (21), an effective diffusivity may be defined as $D_e = D_o I_2^{1/2}$. This is especially convenient because the effective diffusivity may be determined experimentally without detailed knowledge of the particle size and dimensionless viscosity and diffusivity functions. It also does not require that the wall concentration be known. Earlier crossflow microfiltration models have set ϕ_w equal to the particle volume fraction within the cake and thereby imply that the particles are free to diffuse away from the cake without a concentration jump. Here, a jump in concentration is allowed as an approximate model of partially adhesive cakes for which there is an equilibrium between particles on the stagnant cake surface and those adjacent to it within the flowing boundary layer.

It proves convenient to make the governing equations dimensionless by defining $\hat{x} = x/x_{cr}$, $\hat{v}_w = v_w/J_m$, $\hat{J} = J/J_m$, and $\hat{\delta} = \delta_c/H_o$. Then combining Eqs. (11), (12), and (20) yields

$$\frac{1}{\hat{v}_w^2(1-\hat{\delta})^{3n}} = 1 + \int_1^{\hat{x}} \hat{v}_w d\hat{x} \qquad \hat{x} > 1 \quad , \tag{23}$$

$$\hat{J} = \hat{v}_w = \frac{1}{1+\beta\hat{\delta}} \qquad \text{slit} \quad , \tag{24a}$$

$$\hat{J} = (1-\hat{\delta})\hat{v}_w = \frac{1}{1+\beta\ln(1-\hat{\delta})^{-1}} \qquad \text{tube} \quad . \tag{24b}$$

For $\hat{x} \leq 1$, $\hat{\delta} = 0$ and $\hat{J} = 1$. Equation (23) is solved for $\hat{\delta}(\hat{x})$ by substituting in Eq. (24), differentiating the result, and then applying standard numerical rou-

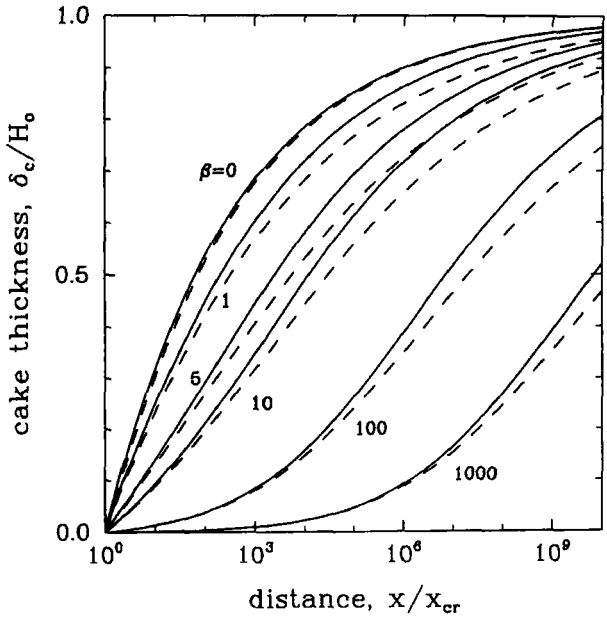

FIGURE 4

The dimensionless cake thickness versus dimensionless distance from the filter entrance for shear–induced diffusion as the dominant back transport mechanism. The solid lines are for rectangular filters and the dashed lines are for cylindrical filters.

tines for first–order nonlinear ordinary differential equations. The dimensionless permeate flux, $\hat{J}(\hat{x})$, is then determined from Eq. (24).

Numerical solutions to Eqs. (23) and (24) for various β are presented in Figures 4 and 5. For small β, the filter cake does not significantly reduce the flux and so it can become very thick and even pinch off the channel. This has been observed by Ofsthun[30] for yeast cakes in narrow hollow fibers. The steady–state cake thickness is reduced by shear–induced diffusion, because the back–diffusion of particles increases due to the increased shear rate as the cake builds up and partially restricts the channel. As β is increased, the flux is decreased due to the

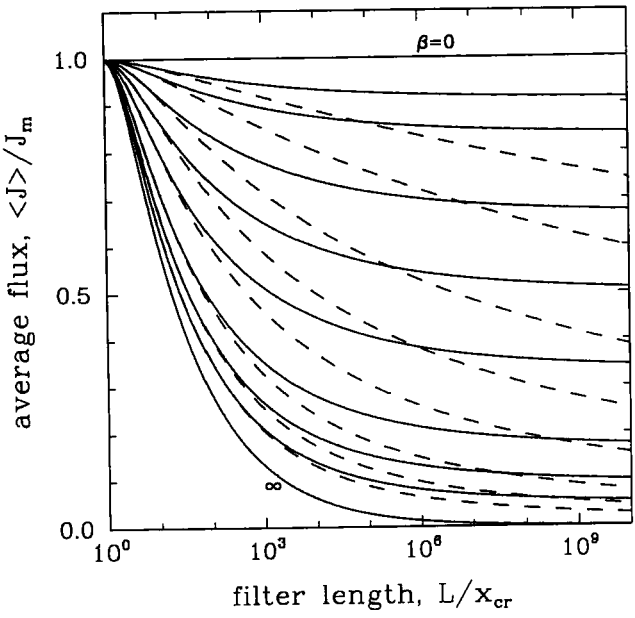

FIGURE 5

The dimensionless, length–averaged permeate flux at steady state versus dimensionless filter length for shear–induced diffusion as the dominant back–transport mechanism. The solid lines are for rectangular filters and the dashed lines are for cylindrical filters. The curves represent the parameter values $\beta = 0$, 0.1, 0.2, 0.5, 1.0, 2.0, 5.0, 10, 20, and ∞, from top to bottom.

increased resistance of the cake layer. The cake thickness also decreases with increasing β, because the reduction in flux implies that less channel constriction is required to achieve a steady–state balance of the deposition of particles into the boundary layer with the convection of these particles toward the filter exit. Good quantitative agreement with these predictions has been observed by Romero and Davis[25] for suspensions of latex spheres.

The cake buildup is less for a tube than for a two–dimensional rectangular channel, because of the greater reduction in cross–sectional area for suspension flow in a tube. However, the steady–state flux is less for a tube than for a

rectangular channel, because of the reduction of surface area for filtration in a tube. The minimum flux for a finite value of β in a tube is $J = 0$, whereas in a rectangular channel it is $J = J_m/(1+\beta)$, corresponding to the tube or channel becoming nearly filled with suspension. For shear–induced diffusion, this occurs only in the limit $x/x_{cr} \to \infty$. In contrast, a tube with only Brownian back-diffusion may become completely blocked off in a finite length for finite β.

Analytical solutions to Eqs. (23) and (24) may be obtained in the limiting cases of membrane–dominated resistance and cake–dominated resistance. In particular, for $\hat{x} > 1$ and membrane–dominated resistance ($\beta \ll 1$):

$$\hat{J} = 1 \quad , \quad \hat{\delta} = 1 - \hat{x}^{-1/6} \quad \text{slit} \quad , \quad \hat{\delta} = 1 - \Big((6\hat{x}+1)/7\Big)^{-1/6} \quad \text{tube} \quad , \tag{25}$$

indicating that the flux remains at its clean membrane value of $J = J_m$, whereas the cake layer thickness builds up to fill an appreciable portion of the tube or channel for $x \gg x_{cr}$. In contrast, for $\hat{x} > 1$ and cake–dominated resistance ($\beta \gg 1$):

$$\hat{J} = (3\hat{x}/2 - 1/2)^{-1/3} \quad , \quad \hat{\delta} = \beta^{-1}\left((3\hat{x}/2 - 1/2)^{1/3} - 1\right) \quad , \tag{26}$$

indicating that the flux is inversely proportional to the one–third power of the distance from the channel entrance for $x \gg x_{cr}$, and that the cake layer remains thin due to its high specific resistance.

The solution for the permeate flux, $J(x)$, may be integrated along the length, L, of a filter in order to find the length–averaged permeate flux. It is this length–averaged flux, $\langle J \rangle$, that is shown in Figure 5. For the dual limit of $\beta \gg 1$ and $L/x_{cr} \gg 1$, which implies that the resistance is dominated by a thin cake over most of the filter length, this yields $\langle \hat{J} \rangle = (3/2)^{2/3}(x_{cr}/L)^{1/3}$, or in dimensional form:

$$\langle J \rangle = 1.31 \left[\frac{\dot{\gamma}_o D_o^2 I_2}{L\phi_b}\right]^{1/3} \quad . \tag{27}$$

The function I_2 depends on ϕ_b, ϕ_w, and the concentration dependencies of the viscosity and diffusion coefficients. For many suspensions, these quantities

(except ϕ_b) are not known or easily determined. Fortunately, they only appear as the single quantity given by Eq. (22). For the special case of constant viscosity and diffusivity, the integrals may be evaluated analytically:

$$I_2 = \phi_w - \phi_b - \phi_b \ln(\phi_w/\phi_b) + \frac{\phi_b}{2}\left(\ln(\phi_w/\phi_b)\right)^2 \quad \text{for } \bar{\mu} = \bar{D} = 1 \quad . \qquad (28)$$

Note that $I_2 = \phi_w$ for dilute suspensions ($\phi_b \ll \phi_w$), and so Eq. (4) is recovered in this limit. For the special case of dilute suspensions of nonadhesive, monodisperse rigid spheres, the numerical value[15] of I_2 is 1×10^{-4}, and Eq. (27) is then identical to Eq. (8).

4 TRANSIENT MODELS FOR THICK CAKE LAYERS

The previous sections describe models for the steady or quasi-steady permeate flux in crossflow microfiltration. In practice, flux decline from the initial value to the steady value is observed over time. Typically, there is a short-term flux decline, occurring over time scales of minutes or hours, due to cake buildup. There is also a long-term flux decline, occurring over time scales of hours or days, due to membrane fouling, membrane compaction, and cake compaction or consolidation. Gradual flux decline also occurs in batch recycle filters due to the gradual increase in the bulk concentration. Both short-term and long-term flux decline may be described by Darcy's law (Eq. (11)), with the cake and membrane resistances being time-dependent. The cake resistance increases as the cake thickness increases, as described by Eq. (12). Moreover, when cake compaction or consolidation occurs, then the specific cake resistance, $\hat{R}_c(t)$, may also increase with time. The membrane resistance, $R_m(t)$, increases with time due to membrane fouling. Petzny and Quinn[31], de Balmann et al.[32], and Robertson and Zydney[33] note that the membrane permeability (the inverse of the specific resistance) may decrease as a result of adsorbed macromolecules

decreasing the effective membrane pore radius. Ethier and Kamm[34,35] have modeled this behavior for rate-limited adsorption in cylindrical pores. Fane[6] and Aimar et al.[36] have measured the changes in membrane resistance due to protein adsorption and observed that it increases from an initial value to a final value in a decaying exponential fashion. Similar observations were made by Matsumoto et al.[37], with the increase in membrane resistance attributed to a pore plugging mechanism. A simple phenomenological expression for this behavior is

$$R_m(t) = R_{mo} + (R_{mf} - R_{mo})\left(1 - \exp(-t/\tau_m)\right) \quad , \tag{29}$$

where R_{mo} is the initial resistance of the clean membrane, R_{mf} is the final resistance of the fouled membrane, and τ_m is a membrane fouling time constant which depends on the concentration of foulant in the feed suspension for adsorption-limited fouling and also on the transmembrane pressure or initial flux for transport-limited fouling. More fundamental expressions for the time rate of change of the membrane resistance are expected to be developed in the future as research on membrane fouling due to adsorption, pore plugging[38], surface deposition[39,40], and other mechanisms proceeds.

In the next subsection, the theory of transient flux decline due to cake buildup during deadend filtration is reviewed. This is followed by a shear-induced diffusion model to describe transient flux decline due to the buildup of the cake layer of rejected particles until the tangential flow of suspension prevents further cake growth. A key result of this model is that the initial transient flux decline due to cake growth in crossflow microfiltration is closely approximated by simple deadend filtration theory. Under conditions for which inertial lift is the primary mechanism for particle back-transport, a model for flux decline due to cake growth may be derived by generalizing the development of Green and Belfort[9], the details of which are omitted here.

4.1 Deadend Filtration Theory for Transient Flux Decline

The rate of cake growth during deadend filtration using a membrane which completely rejects the particles forming the cake may be determined with the aid of a particle mass balance at the edge of the growing cake layer:

$$\left(J + \frac{d\delta_c}{dt}\right) \phi_b = \phi_c \frac{d\delta_c}{dt} \quad , \tag{30}$$

where ϕ_b is the solids volume fraction in the suspension being filtered, and ϕ_c is the solids volume fraction in the cake, just below its top surface. The left-hand-side of Eq. (30) represents the flux of particles into the surface of the cake, and it takes into account that this flux is due to the relative motion of the downward flow of suspension and the upward growth of the cake. As discussed by Doshi and Trettin[41], the contribution to this flux due to back-diffusion of colloidal and fine particles in unstirred cells is negligible. The right-hand-side of Eq. (30) represents the buildup of particles in the cake. Combining Eqs. (11), (12), and (30) yields a first-order ordinary differential equation for the cake-layer thickness on a flat filter:

$$\frac{d\delta_c}{dt} = \frac{\phi_s J}{(\phi_c - \phi_s)} = \frac{\phi_s \Delta p}{(\phi_c - \phi_s)\eta_o(R_m + \hat{R}_c \delta_c)} \quad . \tag{31}$$

This equation is subject to the initial condition, $\delta_c = 0$ at $t = 0$.

Deadend batch filtration is often carried out with a constant imposed pressure drop. In this case, the permeate flux decreases with time due to cake buildup. Eq. (31) may then be separated and integrated to yield

$$R_m \delta_c + \hat{R}_c \frac{\delta_c^2}{2} = \frac{\phi_b \Delta P}{(\phi_c - \phi_s)\mu_o} t \quad . \tag{32}$$

In performing the required integration, it is assumed here that R_m is constant (no significant membrane fouling or compaction over time) and that ϕ_c and $\hat{R}_c$ are constant (no significant changes in cake compression over time), although these assumptions may be relaxed. This quadratic equation is then solved for the cake thickness to yield:

$$\delta_c(t) = \frac{R_m}{\hat{R}_c}\left[\left(1 + \frac{2\hat{R}_c\phi_b\Delta p\, t}{(\phi_c - \phi_b)\mu_o R_m^2}\right)^{1/2} - 1\right] \quad . \tag{33}$$

By combining this with Eq. (34), the flux expression is

$$J(t) = J_m\left(1 + \frac{2\hat{R}_c\phi_b\Delta p\, t}{(\phi_c - \phi_b)\mu_o R_m^2}\right)^{-1/2} \quad , \tag{34}$$

where the initial flux is given by $J_m = \Delta p/\mu_o R_m$. The permeate flux starts at its initial value for a clean membrane and then decreases linearly with time for short times due to cake buildup. As the flux declines, the rate of cake buildup also declines. For long times, the flux is inversely proportional to the square–root of time.

4.2 Shear–induced Diffusion Model for Transient Flux Decline

During crossflow microfiltration, particles will deposit on the membrane surface to form a cake layer, except under extreme conditions (high shear rate, low transmembrane pressure, low feed concentration) for which the particles are convected toward the filter exit by the tangential flow of retentate as rapidly as they are convected toward the membrane surface by the perpendicular flow of permeate. The permeate flux declines according to Darcy's law (Eqs. (11) and (12)) as the cake builds up, and the primary role of the high shear provided by the tangential flow is to arrest the cake buildup. As in the steady–state case, the cake thickness permeate flux may be related to the properties of the concentration polarization boundary layer. The differential mass balances for suspension and particles in the boundary layer are, respectively:

$$\frac{\partial u}{\partial x} + \frac{\partial v}{\partial y} = 0 \quad , \tag{35}$$

$$\frac{\partial c}{\partial t} + \frac{\partial(u\phi)}{\partial x} + \frac{\partial(v\phi)}{\partial y} = \frac{\partial}{\partial y}\left(D\frac{\partial \phi}{\partial y}\right) \quad , \tag{36}$$

where v is the velocity in the transverse (y) direction. The boundary conditions at the outer and inner edges of the boundary layer are

$$\phi = \phi_b \quad , \quad \frac{\partial \phi}{\partial y} = 0 \qquad \text{at } y = \delta_c + \delta \quad , \tag{37a, b}$$

$$u = 0 \ , \ v = -v_w \ , \ \phi = \phi_w \ , \ -v\phi + D\frac{\partial \phi}{\partial y} = (\phi_c - \phi_w)\frac{\partial \delta_c}{\partial t} \quad \text{at } y = \delta_c \ , \tag{37c–f}$$

where $\phi_c = 1 - \epsilon_c$ is the mass concentration of solids in the cake. Instead of solving these equations pointwise, which would be difficult both to perform and to apply in practice, Eq. (36) may be integrated across the boundary layer, yielding[42]:

$$\frac{\partial}{\partial t}\int_{\delta_c}^{\delta_c+\delta} (\phi - \phi_b)dy + (\phi_c - \phi_b)\frac{\partial \delta_c}{\partial t} + \frac{\partial}{\partial x}\int_{\delta_c}^{\delta_c+\delta} u(\phi - \phi_b)dy = v_w\phi_b \quad . \tag{38}$$

The first term in Eq. (38) represents particle accumulation in the boundary layer, the second represents particle accumulation in the cake, the third represents particle convection in the boundary layer by the tangential flow, and the right–hand–side is the convection of particles into the boundary layer due to the permeate flow. After steady–state is reached, the first two terms are zero, and what remains is simply the x–derivative of Eq. (19).

The initial conditions for Eqs. (36) and (38) are that $\phi = \phi_b$ and $\delta_c = 0$ at $t = 0$. Once filtration starts, the particle concentration at the edge of the membrane increases rapidly until it reaches $\phi = \phi_w$ for all $x \geq x_{cr}$ (this typically requires a few seconds). A stagnant cake layer then forms and begins to build up on the membrane surface, because the convection of particles into the boundary layer by the permeate flow (the fourth term in Eq. (38)) exceeds the convection of particles in the boundary layer toward the filter exit by the tangential flow (the third term in Eq. (38)). The capacity of the thin boundary layer for particle accumulation (the first term in Eq. (38)) is typically small. The cake continues to build up until its resistance reduces the permeate flux and its finite thickness constricts the channel, thereby increasing the tangential convection, by sufficient amounts so that the last two terms in Eq. (38) become in balance.

As shown by Romero and Davis[42], the variable of integration may be transformed from y to ϕ, so that Eq. (38) becomes

$$\frac{\partial}{\partial t}\left\{\frac{H_o^n D_o I_1}{(H_o-\delta_c)^n v_w}\right\}+(\phi_c-\phi_b)\frac{\partial \delta_c}{\partial t}+\frac{\partial}{\partial x}\left\{\frac{\dot{\gamma}_o H_o^{3n} D_o^2 I_2}{(H_o-\delta_c)^{3n} v_w^2}\right\}=v_w \quad , \tag{39}$$

where the double integral $I_2(\phi_b, \phi_w)$ is given by Eq. (22), and the single integral $I_1(\phi_b, \phi_w)$ is given by

$$I_1=\int_{\phi_b}^{\phi_w}\frac{(\phi-\phi_b)\bar{D}(\phi)}{\phi}\,d\phi \quad . \tag{40}$$

For constant properties ($\bar{D}=\bar{\mu}=1$), the latter integral is simply $I_1=\phi_w-\phi_b-\phi_b\ln(\phi_w/\phi_b)$.

It proves convenient to nondimensionalize Eq. (39) by defining $\hat{x}=x/x_{cr}$, $\hat{t}=(t-t_{cr})/\tau_c$, $\hat{v}_w=v_w/J_{mo}$ and $\hat{\delta}=\delta_c/H_o$, where $J_{mo}\equiv\Delta p/\mu_o R_{mo}$ is the initial flux and $t_{cr}=D_o I_1/J_{mo}^2$ is the time required for the stagnant cake to first form and is typically negligible[42]. The characteristic time for cake growth, τ_c, is chosen to be the time required for the cake buildup to fill the entire channel, if the flux remained at its initial value and back-diffusion was negligible: $\tau_c\equiv(\phi_\phi-\phi_b)H_o/(\phi_b J_{mo})$. In dimensionless form, Eq. (39) then becomes

$$\frac{1}{Pe}\frac{\partial}{\partial \hat{t}}\left\{\frac{1}{\hat{v}_w(1-\hat{\delta})^n}\right\}+\frac{\partial \hat{\delta}}{\partial \hat{t}}+\frac{\partial}{\partial \hat{x}}\left\{\frac{1}{\hat{v}_w^2(1-\hat{\delta})^{3n}}\right\}=\hat{v}_w \quad , \tag{41}$$

and Eq. (24) is modified to account for internal membrane fouling:

$$\hat{J}=\hat{v}_w=\frac{1}{\alpha+\beta\hat{\delta}} \qquad \text{slit} \quad , \tag{42a}$$

$$\hat{J}=(1-\hat{\delta})\hat{v}_w=\frac{1}{\alpha+\beta\ln(1-\hat{\delta})^{-1}} \qquad \text{tube} \quad , \tag{42b}$$

where $\hat{J}=J/J_{mo}$, $n=2$ for rectangular geometries, $n=3$ for cylindrical geometries, $\alpha=R_m/R_{mo}$, $\beta=H_o\hat{R}_c/R_{mo}$, and R_{mo} is the initial membrane resistance at $\hat{t}=0$. The Péclet number is defined here as $Pe=J_{mo}H_o(\phi_\phi-\phi_b)/D_o I_1$ and is typically much greater than unity, indicating that particle accumulation in the thin flowing polarization layer is small relative to particle accumulation in the stagnant cake layer. Equations (41) and (42) are solved exactly using the method of characteristics[42], as detailed in the Appendix.

The solution strategy outlined in the Appendix may be extended to other cases, including more general situations where R_m and $\hat{R}_c$ are allowed to depend not only on time but also on position and/or intrinsic parameters such as concentration and flux. However, the method of characteristics involves complicated numerical solutions which are unlikely to be applied in practice. Instead, an approximate solution which has its origins in the nature of the characteristics solution is proposed. In particular, the cake buildup and flux decline in the developing region are independent of position and of the imposed crossflow, provided that $Pe \gg 1$ (as is typical). The cake buildup is then governed by deadend filtration theory, which is represented by Eq. (38) with only the middle term retained on its left–hand–side. If we further consider only the typical case of slow membrane fouling and cake compaction relative to the initial rate of cake buildup, then we can set $\alpha = 1$ and $\beta =$ constant in this equation. The resulting solution for rectangular channels and cylindrical tubes are, respectively,

$$\hat{\delta}(t) = \left((1 + 2\beta\hat{t})^{1/2} - 1\right)/\beta \qquad \text{slits} \quad , \quad (43a)$$

$$\frac{1}{2} - \frac{(1-\hat{\delta})^2}{2} + \beta\left(\frac{1}{4} - \frac{(1-\hat{\delta})^2}{4} - \frac{(1-\hat{\delta})^2}{2}\ln(1-\hat{\delta})^{-1}\right) = \hat{t} \qquad \text{tubes} \quad . \quad (43b)$$

Equation (43a) is the dimensionless version of Eq. (33) from deadend filtration theory. This rectangular solution also applies for cylindrical geometries for short times, when $\hat{\delta} \ll 1$.

For the typical condition of a stagnant cake layer forming over most of the filter length ($L/x_{cr} \gg 1$), then the developing solution applies over most of the filter length for short times. The length–averaged, transient permeate flux for short times is then approximated by substituting Eq. (43) into Eq. (42) with $\alpha = 1$:

$$\langle\hat{J}\rangle = 1/\left(1 + 2\beta\hat{t}\right)^{1/2} \quad , \quad (44)$$

which is the dimensionless version of Eq. (34) from deadend filtration theory.

The transient flux decline due to rapid cake buildup continues until the developed region is reached over the entire filter length. After that, a pseudo–steady

state is reached in which flux decline may continue due to gradual membrane fouling and cake compaction. This may be predicted by using the steady-state theory in a quasi-steady fashion, treating $J_m \boxminus \Delta p/\mu_o R_m$ and $\beta \equiv \hat{R}_c H_o/R_m$ as slowly-varying parameters. A recommended approximate model is even simpler—use Eq. (44) to describe the entire transient flux decline, with J_{mo} and β based on $R_m = R_{mo}$, and then use the solution to Eqs. (23) and (24) shown in Figures 4 and 5 (or simply Eq. (27), if $\beta \gg 1$) to describe the steady-state flux, with J_m and β based on $R_m = R_{mf}$. The transient solution is applied until the time at which the flux reaches its steady value. A comparison of this approximate model (dashed lines) with the complete solution (solid lines) using the method of characteristics is shown for a wide range of parameter values in Figures 6–10. The agreement is sufficiently good for the approximate model to be used in practice. In particular, Figure 6 shows that the agreement is excellent for rectangular filters when there is no internal membrane fouling ($\alpha = 1$) or cake compaction (β = constant), and when the concentration polarization boundary layer is very thin ($Pe \to \infty$), for all times and for arbitrary values of the dimensionless cake resistance.

When internal membrane fouling or cake compaction occurs, then there is a period of rapid flux decline due primarily to cake buildup, followed by a period of gradual flux decline due to internal membrane fouling or cake compaction, as shown in Figures 7 and 8. For the typical case of a small characteristic cake growth time relative to the characteristic membrane fouling time, the rapid flux decline closely follows that predicted by the approximate, deadend filtration theory. The subsequent gradual flux decline is not predicted by the approximate theory, which simply sets the flux equal to its steady-state value for the membrane and cake with their final resistances. When the gradual flux decline is severe, this approximation may be improved by applying the steady-state theory in a quasi-steady fashion, using slowly varying membrane and specific cake resistances.

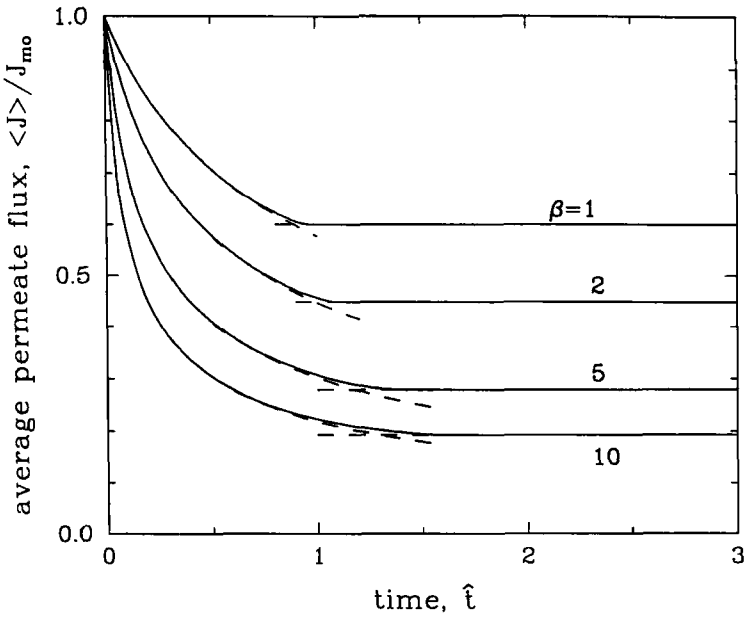

FIGURE 6

The dimensionless length–averaged permeate flux decline for a rectangular filter ($n = 2$) having a nonfouling membrane ($\alpha = 1$) with shear–induced diffusion, $L/x_{cr} = 10^4$, $Pe \to \infty$, and various dimensionless cake resistances. The solid lines are from the exact solution of Eq. (41), whereas the dashed lines are from the approximate solution given by Eq. (43a), together with Eq. (42).

For cylindrical tubes with nonfouling membranes, the predicted flux decline from the complete theory for $Pe \to \infty$ closely follows that from the approximate theory (Eq. (44)) for short times, as demonstrated in Figure 9. For longer times, however, the flux decline from the complete model for $Pe \to \infty$ is more rapid than predicted by the approximate model. This occurs when the cake fills an appreciable fraction of the tube cross–section, so that the curvature correction to Darcy's law becomes important. With this correction, the flux from deadend filtration theory is given by substituting Eq. (43b) into Eq. (42b). The ult is the dotted line in Figure 9, and the agreement with the complete theory is

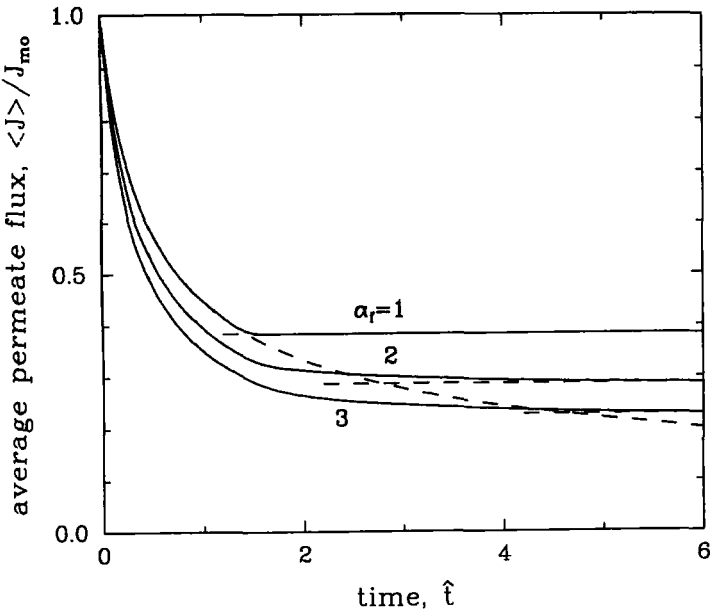

FIGURE 7

The dimensionless length–averaged permeate flux decline for a rectangular filter ($n = 2$) with shear–induced diffusion, $L/x_{cr} = 10^6$, $\beta = 2$, $\hat{\tau}_m = 2$, $Pe \to \infty$, and various dimensionless final membrane resistances. The solid lines are from the exact solution of Eq. (41), whereas the dashed lines are from the approximate solution given by Eq. (43a), together with Eq. (42). Note that the transient portion of the approximate solution does not depend on the final membrane resistance.

excellent for $Pe \to \infty$ up until the time that steady state is reached. Figure 9 also shows how the solution depends on finite values of the Péclet number. When the Péclet number is not large, then significant particle accumulation occurs in the flowing boundary layer, and the cake–layer growth and resulting flux decline occur more slowly. In practice, $Pe \geq 10^2$ for typical parameter values ($J_{mo} = 10^{-2}$ cm/s, $H_o = 0.1$ cm, $D_o = 10^{-5}$ cm^2/s, $\phi_c = 0.6$, $\phi_b = 0.1$, $I_1 = 0.5$), and so this effect is usually small. The good agreement between

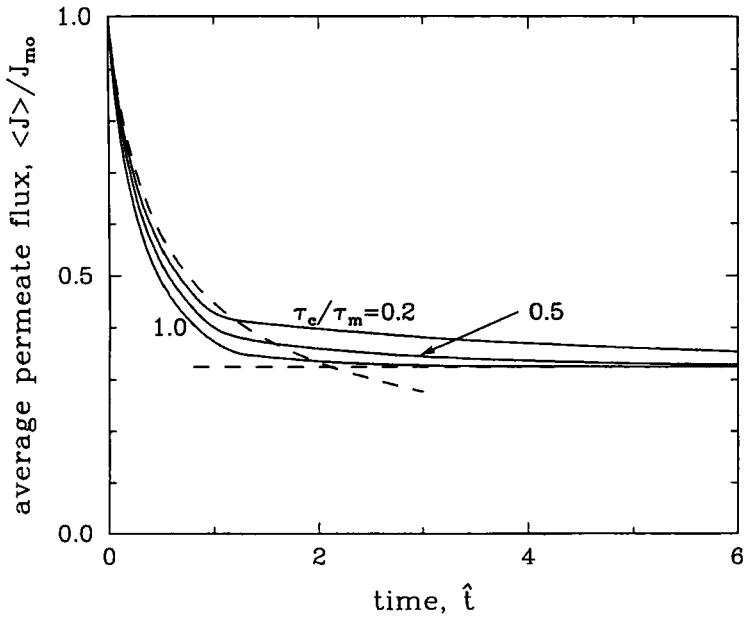

FIGURE 8

The dimensionless length-averaged permeate flux decline for a rectangular filter ($n = 2$) having a fouling membrane ($\alpha_f = 2$) with shear-induced diffusion, $L/x_{cr} = 10^4$, $\beta = 2$, $Pe \to \infty$, and various fouling time constants. The solid lines are from the exact solution of Eq. (41), whereas the dashed lines are from the approximate solution given by Eq. (43a), together with Eq. (42). Note that the approximation solution does not depend on the fouling time constant.

the complete and approximate models for $Pe = 20$ represents a tradeoff of two factors: the accumulation of particles in the boundary layer rather than the cake layer, which increases the flux, and the curvature effect in Darcy's law, which decreases the flux.

Finally, Figure 10 shows the full and approximate solutions for parameter values which are typical of suspensions of micron-sized particles in cylindrical tubes with moderate fouling. The transient flux decline from the complete theory is in close agreement with the approximate, deadend filtration model

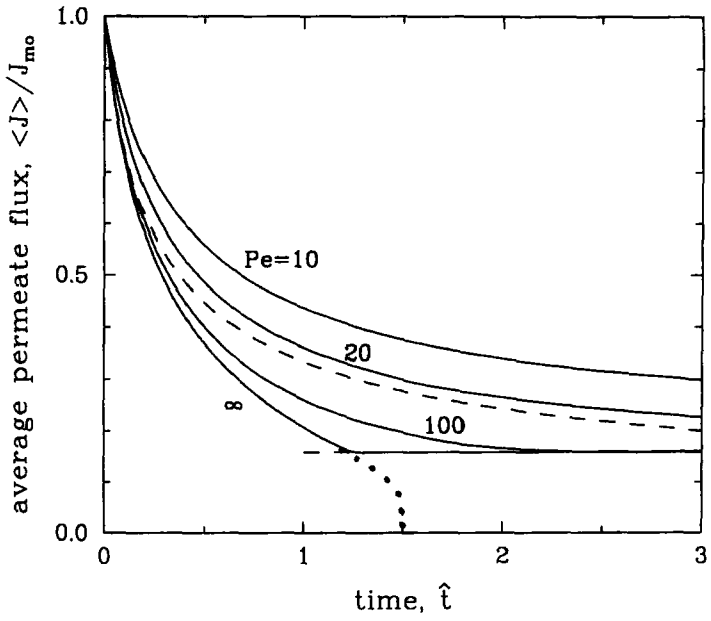

FIGURE 9

The dimensionless length–averaged permeate flux decline for a cylindrical filter ($n = 3$) having a nonfouling membrane ($\alpha = 1$) with shear–induced diffusion, $L/x_{cr} = 10^6$, $\beta = 2$, and various Péclet numbers. The solid lines are from the exact solution of Eq. (41), whereas the dashed and dotted lines are from the approximate solution given by Eqs. (43a) and (43b), respectively, together with Eq. (42). Note that the approximate solution does not depend on the Péclet number.

both with (dotted line) and without (dashed line) the curvature correction, until the flux decreases to less than one–half its initial value. In practice, the dimensionless filter length, L/x_{cr}, may span a wide range of values, but it is typically several orders–of–magnitude larger than unity.

5 CONCLUDING REMARKS

Quasi–steady and transient models for crossflow microfiltration have been developed for typical conditions where both cake resistance and membrane resistance

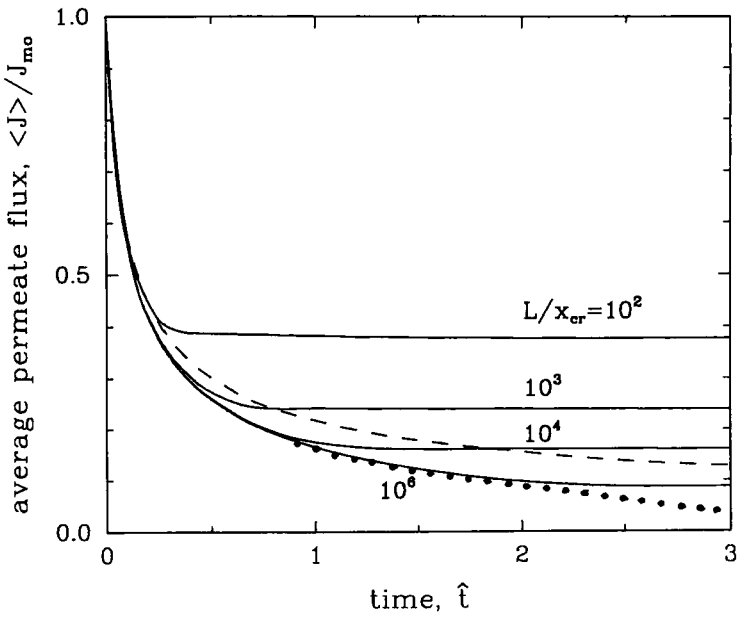

FIGURE 10

The dimensionless length–averaged permeate flux decline for a cylindrical filter ($n = 3$) having a fouling membrane ($\alpha_f = 1.5$ and $\hat{r}_m = 2$) with shear–induced diffusion, $Pe = 10^3$, $\beta = 10$, and various dimensionless filter lengths. The solid lines are from the exact solution of Eq. (41), whereas the dashed and dotted lines are from the approximate solution given by Eqs. (43a) and (43b), respectively, together with Eq. (42). Note that the approximate solution does not depend on the filter length.

contribute to the permeate flux decline. Initially, the rate at which rejected particles are carried toward the membrane by the permeate flow exceeds the rate at which the tangential flow is able to carry them downstream, and so a cake layer builds up on the membrane surface and a concentration polarization layer forms adjacent to it. The cake layer reduces the permeate flux and constricts the channel so that the tangential shear exerted by the bulk suspension increases. This continues until a steady or quasi–steady state is reached in which the rate at which particles are carried into the polarization layer by the permeate

flow is balanced by the rate at which particles are transported away from the cake and are convected downstream by the tangential flow. The back-transport mechanisms considered in this review include Brownian diffusion (submicron particles and low shear rates), inertial lift (supramicron particles and high shear rates), or shear-induced diffusion (intermediate-sized particles and moderate shear rates). In general, cake layers composed of the submicron particles associated with Brownian motion have very high specific resistances and so they remain thin relative to the channel half-height or tube radius. This is also true of highly compressible particles. Under these conditions, the steady or quasi-steady state is reached in a very short time, and the resulting models for thin cake layers are considerably more simple than those for thick cake layers.

If the cake layer is partially adhesive, then there will be a concentration jump at its surface. If the adhesion forces are sufficiently strong, then the particles will stick upon arriving at the cake surface, and there will be no back-diffusion of particles away from the membrane. In this case, a nondiffusive mechanism of particle back-transport is required if cake growth is to be arrested by the shear action of the tangential flow through the tube or channel. One possibility is inertial lift, which becomes important at high shear rates and for particles larger than about ten microns. Another possibility involves particle surface transport, in which the shear exerted by the tangential flow exerts a torque about a contact point on a particle resting on the surface of the cake[43]. If this torque is sufficient to overcome the torques exerted by other contact points, the permeate flow, and any adhesive forces, then the particle would be swept along the cake surface to the filter exit. This would give rise to individual particles rolling along, and perhaps captured by, the surface of the cake. A similar picture would also apply for conditions where the concentration polarization layer thickness, $\delta \approx D/v_w$, is no larger than the diameter of individual particles. Various models which consider the interaction and adhesion of individual particles near the membrane or cake surface have been proposed recently and are able to explain observed data trends when diffusive mechanisms do not apply[43-45].

The rapid flux decline due to cake buildup is followed by a more gradual flux decline due to membrane fouling and/or cake consolidation. The complete shear-induced diffusion model of these effects requires a numerical solution by the method of characteristics. However, it is shown that a simple yet reasonable approximation is to describe the rapid flux decline due to cake buildup by deadend filtration theory—independent of the imposed tangential flow—up until the time at which the predicted steady or quasi-steady flux is reached. A similar conclusion is expected for other back-transport or surface-transport mechanisms occurring as a result of the tangential flow.

The models include physical parameters—such as the membrane resistance (R_m), the specific cake resistance ($\hat{R}_c$), and the crossflow double integral over the concentration-dependence of viscosity and diffusivity (I_2)—which must be determined empirically for particular membranes and suspensions employed in practice. Fortunately, these parameters may be determined from relatively simple experiments. In particular, the membrane resistance may be found from the pure solvent flux. When membrane fouling is severe, the time-dependent membrane resistance may be determined by removing the cake (mechanically or by backflushing) and then measuring the pure-solvent flux at different filtration times.

The specific cake resistance may be determined from fitting the initial transient flux data from a crossflow microfiltration experiment to the deadend filtration theory given by Eq. (34). In particular, the deadend filtration equation may be rearranged in the form:

$$J_m^2/\langle J\rangle^2 = 1 + \frac{2\hat{R}_c\phi_b\Delta p\, t}{(\phi_c - \phi_b)\mu_o R_m^2} \quad , \tag{45}$$

where $J_m = \Delta p/\mu_o R_m$ is the initial flux. Thus, a plot of $J_m^2/\langle J\rangle^2 - 1$ is expected to yield a straight line through the time origin with a slope proportional to the specific cake resistance, $\hat{R}_c$. Since data for the permeate flux generally require that permeate volume versus time data be numerically differentiated, it

is usually more convenient to use the integrated version of the deadend filtration equation:

$$\frac{At}{V} = \frac{\mu_o \hat{R}_c \phi_b V}{2(\phi_c - \phi_b)\Delta p\, A} + \frac{\mu_o R_m}{\Delta p} \quad , \tag{46}$$

where $V(t)$ is the permeate volume collected in time t and A is the membrane area over which the filtration takes place. Thus, a plot of At/V versus V/A is expected to yield a straight line with slope proportional to $\hat{R}_c$ and intercept proportional to R_m (it is still recommended that R_m be determined from pure solvent flux measurements, since the intercept value is very sensitive to uncertainties in the time origin).

The crossflow double integral may be determined from measuring the steady or quasi–steady permeate flux for a given set of operating conditions. In particular, once the length–averaged permeate flux is known, then Figure 5 (or Eq. (27) for cake–dominated resistance) may be used to match theory and experiment to determine I_2 as the only unknown.

Finally, the models described in this review do not explicitly include multiple mechanisms of particle transport away from the cake layer acting simultaneously. A possible improvement to the shear–induced diffusion model would be to include inertial lift by replacing v_w on the right–hand–side of Eqs. (20) and (39) with $v_w - v_L$. This possibility warrants further study and testing with supramicron particles and high shear rates, for which inertial lift is most important. In particular, as the cake layer builds up, the resulting channel constriction increases the effective shear rate at the cake surface. This, in turn, increases both shear–induced diffusion and inertial lift, with the effect on the latter being greater due to the quadratic dependence indicated by Eq. (10).

ACKNOWLEDGEMENTS

A portion of the research described in this review was supported by the Center for Separations Using Thin Films at the University of Colorado, by

Grants CBT–8451014 and CTS-9107703 from the National Science Foundation, and by a fellowship from the Guggenheim Foundation to the author for a portion of the research undertaken while on sabbatical at the Massachusetts Institute of Technology.

APPENDIX

The integral model from Section 4.2 for the transient behavior of crossflow microfiltration has been solved using the method of characteristics by Romero and Davis[42] for the special case of constant membrane resistance. Here, this solution is outlined for the more general case, and illustrative results are presented.

Equations (42) and (43) may be conveniently recast in the following general form:

$$g(\hat{\delta},\alpha,\beta)\,\frac{\partial\hat{\delta}}{\partial\hat{t}} + h(\hat{\delta},\alpha,\beta)\,\frac{\partial\hat{\delta}}{\partial\hat{x}} = f(\hat{\delta},\alpha,\beta) \quad , \tag{47}$$

where α and β may increase with time due to membrane fouling and cake compaction or consolidation, respectively, and may also depend on operating conditions such as concentration and transmembrane pressure.

The functions f, g, and h are given by

$$f = \frac{1}{\alpha+\beta\hat{\delta}} - \frac{2(\alpha+\beta\hat{\delta})(\partial\alpha/\partial\hat{x}+\hat{\delta}\partial\beta/\partial\hat{x})}{(1-\hat{\delta})^{3n}}$$

$$-\frac{1}{Pe}\,\frac{(\partial\alpha/\partial\hat{t}+\hat{\delta}\partial\beta/\partial\hat{t})}{(1-\hat{\delta})^{n}} \qquad \text{slit } (n=2) \quad , \tag{48a}$$

$$f = \frac{1}{(1-\hat{\delta})(\alpha+\beta\ln(1-\hat{\delta})^{-1})}$$

$$-\frac{2(\alpha+\beta\ln(1-\hat{\delta})^{-1})(\partial\alpha/\partial\hat{x}+\ln(1-\hat{\delta})^{-1}\partial\beta/\partial\hat{x})}{(1-\hat{\delta})^{3n-2}}$$

$$-\frac{1}{Pe}\,\frac{(\partial\alpha/\partial\hat{t}+\ln(1-\hat{\delta})^{-1}\partial\beta/\partial\hat{t})}{(1-\hat{\delta})^{n-1}} \qquad \text{tube } (n=3) \quad , \tag{48b}$$

$$g = 1 + \frac{1}{Pe}\left\{\frac{\beta}{(1-\hat{\delta})^n} + \frac{n(\alpha+\beta\hat{\delta})}{(1-\hat{\delta})^{n+1}}\right\} \qquad \text{slit } (n=2) \quad , \quad (49a)$$

$$g = 1 + \frac{1}{Pe}\left\{\frac{\beta}{(1-\hat{\delta})^n} + \frac{(n-1)(\alpha+\beta\ln(1-\hat{\delta})^{-1})}{(1-\hat{\delta})^{n-2}}\right\} \qquad \text{tube } (n=3) \quad , \quad (49b)$$

$$h = \frac{2\beta(\alpha+\beta\hat{\delta})}{(1-\hat{\delta})^{3n}} + \frac{3n(\alpha+\beta\hat{\delta})^2}{(1-\hat{\delta})^{3n+1}} \qquad \text{slit } (n=2) \quad , \quad (50a)$$

$$h = \frac{2\beta(\alpha+\beta\ln(1-\hat{\delta})^{-1})}{(1-\hat{\delta})^{3n-1}} + \frac{(\alpha+\beta\ln(1-\hat{\delta})^{-1})^2(3n-2)}{(1-\hat{\delta})^{3n-3}} \qquad \text{tube } (n=3) \quad , \quad (50b)$$

where α and β are allowed to vary with both time and position for the general case.

The initial and boundary conditions for Eq. (47) are:

$$\hat{\delta} = 0 \quad , \quad \hat{t} \leq 0 \quad \text{for} \quad \hat{x} \geq 0 \quad , \qquad (51a)$$

$$\hat{\delta} = 0 \quad , \quad \hat{x} \leq 1 \quad \text{for} \quad \hat{t} \geq 0 \quad . \qquad (51b)$$

These equations are solved using the method of characteristics. In the developing region, the characteristic lines are governed by

$$d\hat{x}/d\hat{t} = h/g \quad , \quad \hat{x} = \hat{x}_o \ \text{at} \ \hat{t} = 0 \quad , \qquad (52)$$

and the solution along these characteristics is governed by

$$d\hat{\delta}/d\hat{t} = f/g \quad , \quad \hat{\delta} = 0 \ \text{at} \ \hat{t} = 0 \quad . \qquad (53)$$

In the developed region, these equations are replaced by

$$d\hat{t}/d\hat{x} = g/h \quad , \quad \hat{t} = \hat{t}_o \ \text{at} \ \hat{x} = 1 \quad , \qquad (54)$$

$$d\hat{\delta}/d\hat{x} = f/h \quad , \quad \hat{\delta} = 0 \ \text{at} \ \hat{x} = 1 \quad . \qquad (55)$$

The developing and developed regions are separated by the primary characteristic, having $\hat{x}_o = 1$ and $\hat{t}_o = 0$. Once these equations are solved, the solution in real time and space, $\hat{\delta}(\hat{x}, \hat{t})$, is obtained from the solution along the characteristics, $\hat{\delta}(\hat{t}, \hat{x}_o)$ or $\hat{\delta}(\hat{x}, \hat{t}_o)$, by using the characteristic lines, $\hat{x}(\hat{t}, \hat{x}_o)$ or $\hat{t}(\hat{x}, \hat{t}_o)$, to relate real time and space to characteristic time and space in the developing and developed regions, respectively.

The solution by the method of characteristics is illustrated in Figures 11–16. For these figures, the exponential decay function given by Eq. (29) to describe the increase in membrane resistance due to fouling is used. In dimensionless form, this yields

$$\alpha(t) = 1 + (\alpha_f - 1)(1 - e^{-\hat{t}/\hat{\tau}_m}) \quad , \tag{56}$$

where $\alpha_f \equiv R_{mf}/R_{mo}$, with R_{mf} being the final membrane resistance, and $\hat{\tau}_m = \tau_m/\tau_c$, with τ_m being the characteristic membrane fouling time. Also, a constant value of $\beta = 5.0$ was used, the Péclet number was set at infinity, and a cylindrical tube ($n = 3$) with shear–induced diffusion was analyzed (but without the correction for curvation in Darcy's law). A second–order Euler method with logarithmic spatial steps and linear time steps was used to numerically solve the nonlinear, first–order ordinary differential equations. The resulting map of characteristic lines is shown in Figure 11. The dotted curves are the characteristics determined from Eq. (52) for the developing region, whereas the dashed curves are the characteristics determined from Eq. (54) for the developed region. The solid curve is the primary characteristic. Figure 12 shows the dimensionless cake thickness and permeate flux along the developing characteristics. Note that the solution along all characteristics collapse onto a single curve, because the functions f and g required in Eq. (53) depend explicitly on $\hat{\delta}$ and $\hat{t}$, but not $\hat{x}$. This has the important consequence that cake buildup and flux decline in the developing region depend on time but not position in the filter. Figure 13 shows the dimensionless cake thickness and permeate flux along the developed characteristics. In this case, the solution differs along the different characteristic

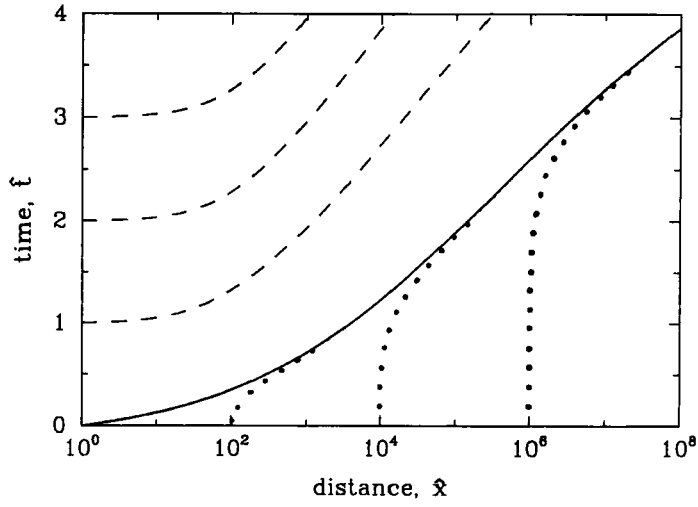

FIGURE 11

Characteristic map for a cylindrical tube ($n = 3$) with shear–induced diffusion, $Pe \to \infty$, $\beta = 5$, $\alpha_f = 5$, and $\tau_c/\tau_m = 1$. The solid curve is the primary characteristic, the dotted curves are the developing characteristics, and the dashed curves are the developed characteristics.

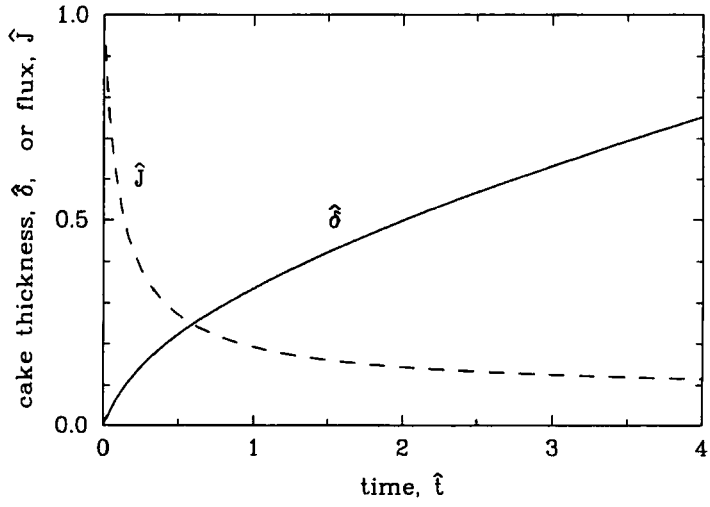

FIGURE 12

Dimensionless cake thickness (solid line) and permeate flux (dashed line) along developing characteristics for the conditions of Figure 11.

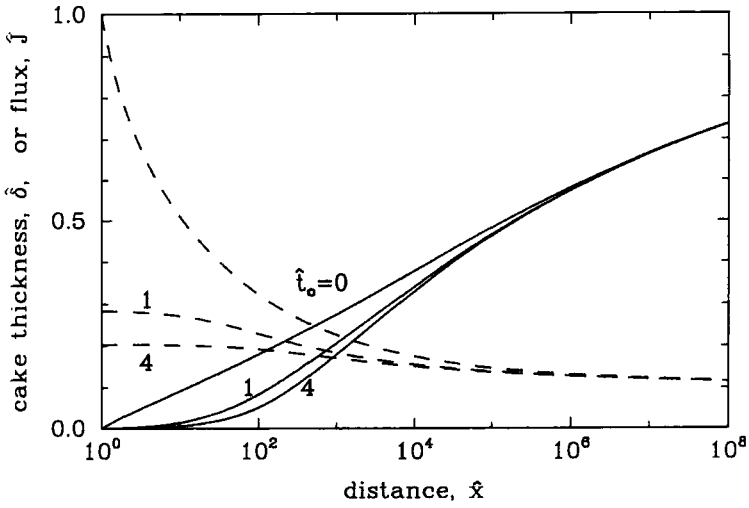

FIGURE 13

Dimensionless cake thickness (solid lines) and permeate flux (dashed lines) along developed characteristics for the conditions of Figure 11.

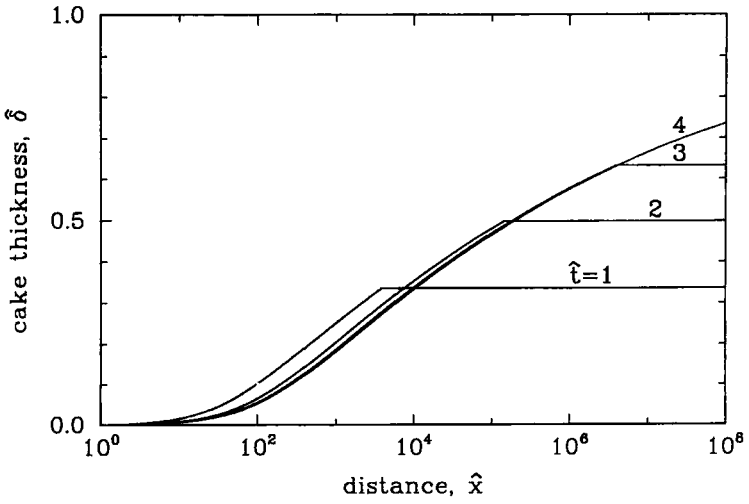

FIGURE 14

Dimensionless cake thickness versus distance for various times and the conditions of Figure 11.

lines, because membrane fouling causes the functions f and h appearing in Eq. (55) to depend explicitly on $\hat{t}$.

Using the characteristic solution, Figures 14 and 15 were constructed to show the solution in real time and space. Note from Figure 14 that the cake thickness at a given time increases monotonically with distance in the developed region near the filter entrance, but that it is independent of position in the developing region further down the channel. Moreover, the cake thickness increases with time, as expected, in the developing portion of the filter, whereas it actually decreases with time in the developed portion of the filter. This surprising feature is shown more clearly in Figure 15, where the cake is seen to build up with time in the developing region, independent of position, and then to erode with time in the developed region. The physical explanation for this is that the rate at which particles are carried into the boundary layer by the permeate flow in the

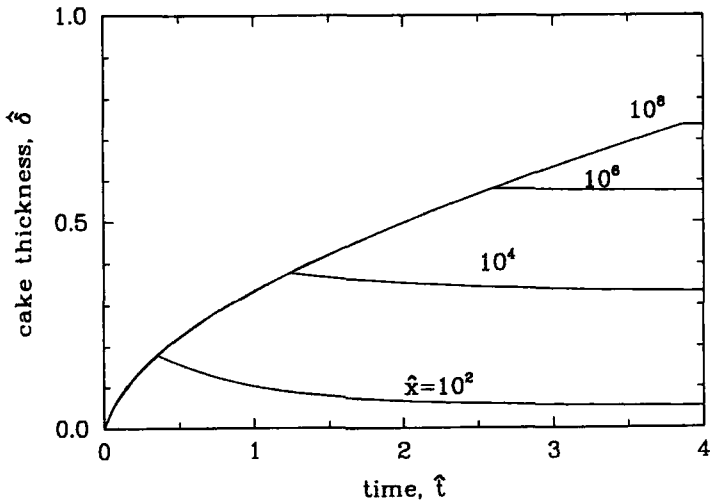

FIGURE 15

Dimensionless cake thickness versus time for various distances and the conditions of Figure 11.

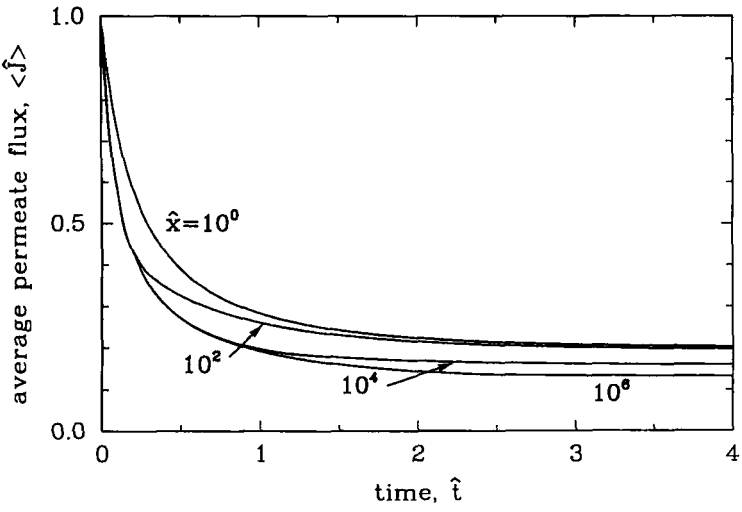

FIGURE 16

The dimensionless length–averaged permeate versus time for filters of different lengths and the conditions of Figure 11.

developing region exceeds the ability of the particles to diffuse away from the cake and be convected downstream by the tangential flow. As a result, the cake thickness increases with time in the developing region, thereby reducing the permeate flux and increasing the tangential shear rate, until a balance is achieved for particle flux toward and away from the cake layer. After this time, the developed solution applies. However, the permeate flux continues to decline due to internal membrane fouling. This reduces the rate at which particles are convected toward the cake by the permeate flow, below the rate at which they diffuse away from the cake and are convected downstream, and so the cake erodes. Such erosion has been observed by Ofsthun[30] using freeze–substitution methods for microfiltration of yeast and protein mixtures in hollow fibers. Of course, for particles which are adhesive, so that cake buildup is irreversible, the cake thickness will remain constant with time in the developed portion, and the permeate flux from then on will be given by Eq. (42) with $\hat{\delta}$ fixed but with α

(and β) changing with time due to membrane fouling (and cake compaction). Finally, the length-averaged permeate flux decline is shown in Figure 16 for different filter lengths. Note that the initial flux decline is independent of filter length, except for very short filters.

NOMENCLATURE

a	particle radius, μm
b	dimensionless function in Eq. (9)
D	diffusion coefficient, cm^2/s
D_B	Brownian diffusion coefficient, given by Eq. (3), cm^2/s
D_o	characteristic shear-induced diffusion coefficient, $a^2\dot{\gamma}_o$, cm^2/s
D_s	shear-induced diffusion coefficient, approximated by Eq. (5), cm^2/s
$\bar{D}$	dimensionless diffusion coefficient, $(H_o - \delta_c)^n D/H_o^n D_o$
f	dimensionless function defined by Eq. (48)
g	dimensionless function defined by Eq. (49)
h	dimensionless function defined by Eq. (50)
H	channel half-height or tube radius, cm
I_1	dimensionless single crossflow integral defined by Eq. (40)
I_2	dimensionless double crossflow integral defined by Eq. (22)
J	permeate flux, cm/s
$\langle J \rangle$	length-averaged permeate flux, cm/s
J_m	permeate flux for membrane resistance only, $\Delta p/\mu_o R_m$, cm/s
$\hat{J}$	dimensionless permeate flux, J/J_m
k	Boltzmann's constant, 1.38×10^{-16} g-cm^2/s^2-°K
K	dimensionless constant in Eq. (14)
L	filter length, cm
n	parameter with value 2 (rectangular slit) or 3 (cylindrical tube)

Δp	transmembrane pressure drop, g/cm–s^2
Pe	dimensionless Péclet number, $J_{mo}H_o(\phi_c - \phi_b)/D_oI_1$
Q	feed flow rate, cm^3/s
$\hat{Q}$	dimensionless excess particle flux defined following Eq. (22)
R_c	cake resistance, cm^{-1}
$\hat{R}_c$	specific cake resistance per unit height, cm^{-2}
R'_c	specific cake resistance per unit mass per unit area, cm/g
R_m	membrane resistance, cm^{-1}
S_c	solids surface area per volume of solids, cm^{-1}
t	time, s
t_{cr}	time for cake layer to first form, D_oI_1/J_{mo}^2, s
$\hat{t}$	dimensionless time, $(t - t_{cr})/\tau_c$
T	absolute temperature, °K
u	axial velocity component, cm/s
v	transverse velocity component, cm/s
v_w	permeate velocity at edge of cake, cm/s
$\hat{v}_w$	dimensionless permeate velocity, v_w/J_{mo}
v_L	inertial lift velocity, defined by Eq. (16), cm/s
$v_{L,o}$	inertial lift velocity in absence of cake layer, defined by Eq. (9), cm/s
W	width of rectangular filter, cm
x	axial distance from filter entrance, cm
x_{cr}	position where cake first forms, defined by Eq. (21), cm
$\hat{x}$	dimensionless distance, x/x_{cr}
y	transverse distance from membrane surface, cm

Greek symbols

α	dimensionless membrane resistance, R_m/R_{mo}
β	dimensionless cake resistance, $\hat{R}_cH_o/R_m$
δ	concentration polarization boundary layer thickness, cm

δ_c	cake layer thickness, cm
$\hat{\delta}$	dimensionless cake layer thickness, δ_c/H_o
ϵ	void fraction
$\dot{\gamma}_o$	shear rate at membrane surface, given by Eq. (2), s^{-1}
μ	suspension viscosity, g/cm–s
μ_o	pure fluid viscosity, g/cm–s
$\bar{\mu}$	dimensionless suspension viscosity, μ/μ_o
ϕ	particle volume fraction, $1-\epsilon$
ρ_o	pure fluid density, g/cm^3
ρ_s	solid particle density, g/cm^3
τ_c	characteristic time for cake buildup, $(\phi_c-\phi_b)H_o/(\phi_b J_{mo})$
τ_m	characteristic time for membrane fouling, defined by Eq. (29), s
$\hat{\tau}_m$	dimensionless membrane fouling time, τ_m/τ_c

Subscripts

b	bulk suspension
c	cake layer
f	final conditions
m	membrane
o	initial conditions in absence of cake layer, or pure fluid values
w	edge of boundary layer, just above cake layer

REFERENCES

1. W. F. Blatt, A. Dravid, A. S. Michaels, and L. Nelson, in *Membrane Science and Technology*, J. E. Flinn, ed., Plenum Press, New York, 1970, pp. 47–97.

2. J. D. Henry, in *Recent Developments in Separations Science*, Second Edition, N. N. Li, ed., CRC Press, Cleveland, 1972, pp. 205–225.

3. M.C. Porter, *Ind. Eng. Chem. Prod. Res. Dev.* **11**, 233-248 (1972a).
4. M. C. Porter, in *Recent Advances in Separation Techniques, AIChE Symp. Ser. Vol. 68, No. 120*, 1972b, pp. 21–30.
5. M. C. Porter, in *Synthetic Membranes: Science, Engineering and Applications*, P. M. Bungay, H. K. Lonsdale, and M. N. de Pinho, eds., Dordrect, D. Reidel, 1986, pp. 225–246.
6. A. G. Fane, in *Progress in Filtration and Separation*, Vol. IV, R. J. Wakeman, ed., Elsevier, 1986, pp. 101–179.
7. G. Belfort, *J. Membrane Sci.* **40**, 123–147 (1989).
8. D. R. Trettin and M. R. Doshi, *Chem. Eng. Commun.* **4**, 507–522 (1980).
9. G. Green and G. Belfort, *Desalination* **35**, 129–147 (1980).
10. A. L. Zydney and C. K. Colton, *Chem. Eng. Commun.* **47**, 1–21 (1986).
11. E. C. Eckstein, P. G. Bailey and A. H. Shapiro, *J. Fluid Mech.* **79**, 191–208 (1977).
12. R. H. Davis and J. D. Sherwood, *Chem. Eng. Sci.* **45**, 3203–3209 (1990).
13. D. T. Leighton and A. Acrivos, *J. Fluid Mech.* **177**, 109–131 (1987a).
14. D. T. Leighton and A. Acrivos, *J. Fluid Mech.* **181**, 415–439 (1987b).
15. R. H. Davis and D. T. Leighton, *Chem. Eng. Sci.* **42**, 275–281 (1987).
16. R. E. Madsen, "Hyperfiltration and Ultrafiltration in Plate–and–Frame Systems," New York, Elsevier, 1977.
17. F. W. Altena and G. Belfort, *Chem. Eng. Sci.* **39**, 343–355 (1984).
18. G. Belfort and N. Nagata, *Desalination* **53**, 57–79 (1985).
19. G. Belfort, R. J. Weigand, and J. T. Mahar, in *ACS Symp. Ser. No. 281: Reverse Osmosis and Ultrafiltration*, S. Sourirajan and T. Matsuura, eds., 1985, pp. 383–401.
20. J. R. Otis, F. W. Altena, J. T. Mahar, and G. Belfort, *Expl. Fluids* **4**, 1–10 (1986).
21. B. P. Ho and L. G. Leal, *J. Fluid Mech.* **65**, 365–400 (1974).

22. K. Ishii and H. Hasimoto, *J. Phys. Soc. of Japan* **48**, 2144–2153 (1980).

23. D. A. Drew, J. A. Schonberg, and G. Belfort, *Chem. Eng. Sci.* **46**, 3219–3224 (1991).

24. A. L. Zydney and C. K. Colton, in *Proc. International Symp. on Artificial Organs, Biomedical Engineering and Transplantation*, J. D. Andrade et al., eds., VCH Publishers, Inc., New York, 1987, pp. 343–358.

25. C. A. Romero and R. H. Davis, *J. Memb. Sci.* **62**, 249–273 (1991).

26. M. C. Porter, in *What the Filter Man Needs to Know About Filtration, AIChE Symp. Ser. Vol. 73, No. 171*, W. Shoemaker, ed., 1977, pp. 83–103.

27. P. C. Carman, *Trans. Inst. Chem. Eng.* **16**, 168–187 (1938).

28. H. P. Grace, *Chem. Eng. Prog.* **49**, 303–318 (1953).

29. C. A. Romero and R. H. Davis, *J. Memb. Sci.* **39**, 157–185 (1988).

30. N. J. Ofsthun, "Crossflow Membrane Filtration of Cell Suspensions," Ph.D. Thesis, Massachusetts Institute of Technology, Chemical Engineering Department, Cambridge, Massachusetts, 1989.

31. R. J. Petzny and J. A. Quinn, *Science* **166**, 751–753 (1969).

32. H. de Balmann, M. Meireles, P. Aimar, and V. Sanchez, in *Advances in Reverse Osmosis and Ultrafiltration*, T. Matsuura and S. Sourirajan. eds., Nat. Res. Council Canada, 1989, pp. 215–235.

33. B. C. Robertson and A. L. Zydney, *J. Colloid Interf. Sci.* **134**, 563–575 (1990).

34. C. R. Ethier and R. D. Kamm, *PhysicoChem. Hydrodyn.* **11**, 205–217 (1989a).

35. C. R. Ethier and R. D. Kamm, *PhysicoChem. Hydrodyn.* **11**, 219–227 (1989b).

36. P. Aimar, S. Baklouti, and V. Sanchez, *J. Memb. Sci.* **29**, 207–224 (1986).

37. Y. Matsumoto, S. Nakao, and S. Kimura, *Int. Chem. Eng.* **28**, 677–683 (1988).

38. C. Visvanathan and R. B. Aim, *J. Memb. Sci.* **45**, 3–15 (1989).

39. W. S. Opong and A. L. Zydney, *J. Colloid Interf. Sci.* **142**, 41–60 (1991).

40. K. J. Kim, A. G. Fane, C. J. D. Fell, and D. C. Joy, *J. Memb. Sci.* **68**, 79–91 (1992).

41. M. R. Doshi and D. R. Trettin, *Ind. Eng. Chem. Fundam.* **20**, 221–229 (1981).

42. C. A. Romero and R. H. Davis, *Chem. Eng. Sci.* **45**, 13–25 (1990).

43. W.–M. Lu and S.–C. Ju, *Sep. Sci. Tech.* **24**, 517–540 (1989).

44. M. R. Mackley and N. E. Sherman, *Chem. Eng. Sci.* (in press).

45. K. Stamatakis and C. Tien, *AIChE J.* (in press).